The Hydrological Modeling and Analysis Platform (HyMAP): Evaluation in the Amazon Basin

A. C. V. Getirana, A. Boone, D. Yamazaki, B. Decharme, F. Papa, N. Mognard

▶ **To cite this version:**

A. C. V. Getirana, A. Boone, D. Yamazaki, B. Decharme, F. Papa, et al.. The Hydrological Modeling and Analysis Platform (HyMAP): Evaluation in the Amazon Basin. Journal of Hydrometeorology, 2012, 13 (6), pp.1641-1665. 10.1175/jhm-d-12-021.1 . hal-00991053

HAL Id: hal-00991053
https://hal.science/hal-00991053

Submitted on 16 May 2014

HAL is a multi-disciplinary open access archive for the deposit and dissemination of scientific research documents, whether they are published or not. The documents may come from teaching and research institutions in France or abroad, or from public or private research centers.

L'archive ouverte pluridisciplinaire **HAL**, est destinée au dépôt et à la diffusion de documents scientifiques de niveau recherche, publiés ou non, émanant des établissements d'enseignement et de recherche français ou étrangers, des laboratoires publics ou privés.

The Hydrological Modeling and Analysis Platform (HyMAP): Evaluation in the Amazon Basin

AUGUSTO C. V. GETIRANA*

LEGOS/CNES-CNRS-IRD-UPS, and CNRM-GAME/Météo-France, Toulouse, France

AARON BOONE

CNRM-GAME/Météo-France, Toulouse, France

DAI YAMAZAKI

University of Tokyo, Tokyo, Japan

BERTRAND DECHARME

CNRM-GAME/Météo-France, Toulouse, France

FABRICE PAPA AND NELLY MOGNARD

LEGOS/CNES-CNRS-IRD-UPS, Toulouse, France

(Manuscript received 7 February 2012, in final form 12 June 2012)

ABSTRACT

Recent advances in global flow routing schemes have shown the importance of using high-resolution topography for representing floodplain inundation dynamics more reliably. This study presents and evaluates the Hydrological Modeling and Analysis Platform (HyMAP), which is a global flow routing scheme specifically designed to bridge the gap between current state-of-the-art global flow routing schemes by combining their main features and introducing new features to better capture floodplain dynamics. The ultimate goals of HyMAP are to provide the scientific community with a novel scheme suited to the assimilation of satellite altimetry data for global water discharge forecasts and a model that can be potentially coupled with atmospheric models. In this first model evaluation, HyMAP is coupled with the Interactions between Soil–Biosphere–Atmosphere (ISBA) land surface model in order to simulate the surface water dynamics in the Amazon basin. The model is evaluated over the 1986–2006 period against an unprecedented source of information, including in situ and satellite-based datasets of water discharge and level, flow velocity, and floodplain extent. Results show that the model can satisfactorily simulate the large-scale features of the water surface dynamics of the Amazon River basin. Among all stream gauges considered, 23% have Nash–Sutcliffe coefficients (NS) higher than 0.50 and 68% above zero. About 28% of the stations have volume errors lower than 15%. Simulated discharges at Óbidos had NS = 0.89. Time series of simulated floodplains at the basin scale agrees well with satellite-based estimates, with a relative error of 7% and correlation of 0.89. These results indicate nonnegligible improvements in comparison to previous studies for the same region.

1. Introduction

A better understanding of freshwater flux and storage over the continents has been the subject of numerous studies in the last few decades. Indeed, understanding surface water dynamics (including floodplain, wetlands, inundations, etc.) is fundamental given its role in the continental water and energy cycle. For instance, it has

* Current affiliation: Hydrological Sciences Laboratory, NASA Goddard Space Flight Center, Greenbelt, Maryland.

Corresponding author address: Augusto Getirana, Hydrological Sciences Laboratory, NASA Goddard Space Flight Center, 8800 Greenbelt Road, Greenbelt, MD 22071.
E-mail: augusto.getirana@nasa.gov

DOI: 10.1175/JHM-D-12-021.1

© 2012 American Meteorological Society

been demonstrated that wetland areas, covering about 5% of the earth's land surface (Prigent et al. 2007), can play an important role within the climate system variability. Continental surface waters also influence the surface energy balance and feedback effects between the land surface and atmosphere (Krinner 2003; Mohamed et al. 2005). They also play an important role on water discharges of large rivers, sediment dynamics (Dunne et al. 1998), and freshwater chemistry (e.g., Melack et al. 2004). Finally, wetlands have been shown to have a significant impact on the interannual variability of global methane emissions (Bousquet et al. 2006).

The numerical modeling of the horizontal fluxes of land surface waters is traditionally performed by flow routing schemes (FRSs), which are often driven by surface runoff R and subsurface runoff (or baseflow, B) rates derived from land surface models (LSMs), or coupled with hydrological models composed of simplified vertical energy and water balance schemes.

The first attempts in simulating global land surface hydrology were based on linear relationships between water volume storage and discharge, assuming linear reservoirs with constant residence times (e.g., Vörösmarty et al. 1989), constant (e.g., Oki and Sud 1998), and variable flow velocity v based on empirical equations based on river morphology and topography gradient (e.g., Miller et al. 1994). The coarse spatial resolutions used by these models, varying between 0.5° and 2.5°, were mainly due to computational limitations or in order for the models to be compatible with typical general circulation models (GCMs) at that time.

Recent studies have improved the parameterization of FRS by considering the flow routing at the subgrid scale using linear reservoirs; flow routing between grid cells based on simplified formulations of the Saint–Venant equations, such as the kinematic and diffusive wave equations; interactions between rivers and floodplains; and evaporation from open waters (Döll et al. 2003; Decharme et al. 2012; Yamazaki et al. 2011). Also, recent advances in data availability, resolution, and processing allow one to simulate land surface hydrology globally at a 0.25°–0.50° spatial resolution and subdaily time steps. In particular, a few parameterizations can represent floodplain dynamics in FRS by taking into account topographic information from high-resolution digital elevation models (DEMs) in order to characterize the flooded area × water height relation within a grid cell. These schemes are based on statistical functions (e.g., Coe et al. 2008; Dadson et al. 2010) or elevation profiles (Decharme et al. 2012; Yamazaki et al. 2011), and are able to represent both the water storage and water fluxes between rivers and floodplains within a grid cell at the large scale. However, they still do not account for water fluxes through inundated areas. On the other hand, it has been demonstrated that floodplains can alter the water transport in large basins such as the Amazon basin (Richey et al. 1989). This physical process is explicitly represented by meso- and regional-scale hydrodynamic models (e.g., Estrela and Quintas 1994; Horritt and Bates 2002; Biancamaria et al. 2009; Paiva et al. 2012), but the application of such approaches at the global scale is computationally prohibitive.

While coupling LSMs and FRSs in online mode can require complex programming, the implementation of offline LSM–FRS systems is a straightforward solution for reproducing horizontal water fluxes from LSM outputs over the continents. The offline mode coupling consists in, as a first step, running a given LSM and then, as a postprocessing step, using R and B derived from the land surface model as inputs of the FRS. This two-step procedure allows one to promptly convert runoff from any land surface model into streamflow. On the other hand, offline mode runs prevent LSMs from benefitting from FRS feedbacks, such as the spatiotemporal distribution of wetlands and flooded zones, which could account for a better simulation of evapotranspiration and soil moisture—particularly, considering that evaporation from floodplains in the vertical water and energy balance of an LSM can significantly improve water discharge simulations, as demonstrated by Decharme et al. (2012).

The aforementioned issues are addressed in the present paper. A new global FRS, the Hydrological Modeling and Analysis Platform (HyMAP), is presented and evaluated. HyMAP was specially developed to route LSM outputs in offline mode, taking into account water surface dynamics and representing the runoff and baseflow time delays, the interaction between rivers and floodplains, floodplain water flow among grid cells, and evaporation from open waters.

As a first experiment, HyMAP is coupled with the Interactions between Soil–Biosphere–Atmosphere (ISBA) LSM (Noilhan and Mahfouf 1996) in offline mode and has its performance evaluated in the Amazon basin over the 1986–2006 period at 0.25° spatial resolution. The Princeton University 3-hourly atmospheric dataset (Sheffield et al. 2006) is used as input to force the system. The model is extensively evaluated using both in situ and satellite-based observations, including in situ water discharge and flow velocity made available by the Brazilian Water Agency [Agência Nacional de Águas (ANA)], along with radar altimetry data acquired by *Envisat* and multisatellite-derived estimates of inundation extent at a 0.25° spatial resolution (Prigent et al. 2007; Papa et al. 2010). This paper is organized into five sections. Section 2 presents a detailed description of HyMAP and the model parameterization. The

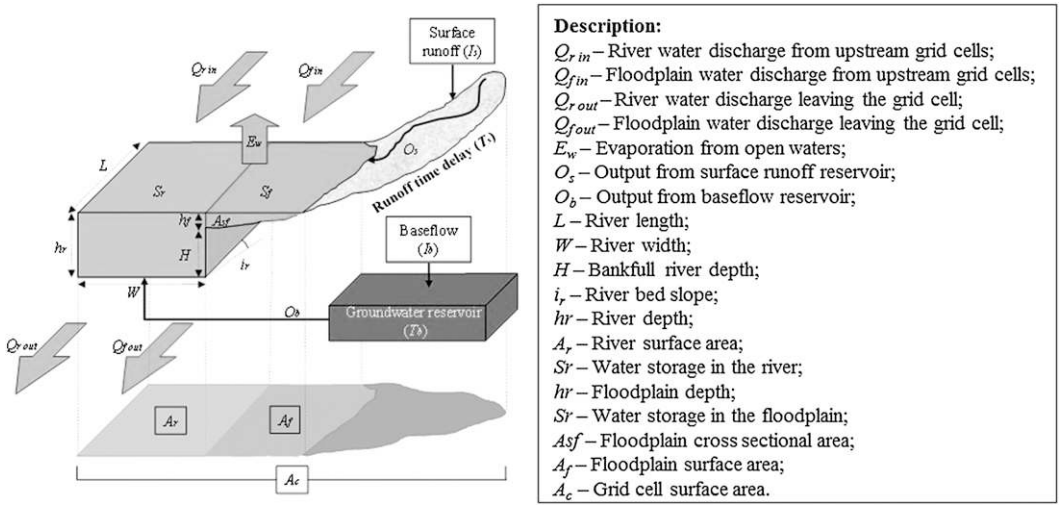

FIG. 1. Schematic of a river channel reservoir and a floodplain reservoir within a grid cell as represented in HyMAP.

experimental design, forcings, and evaluation datasets are described in section 3. Results and discussion are shown in section 4, and the conclusions are provided in section 5.

2. HyMAP: The Hydrological Modeling and Analysis Platform

HyMAP is a global-scale flow routing scheme specifically designed to be coupled with any LSM in offline mode. The model has been developed in the framework of the future Surface Water and Ocean Topography (SWOT) mission, planned to be launched within the decade and which will provide high-resolution characterization of water surface elevations with two-dimensional global maps of terrestrial surface water extent and storage changes (Alsdorf et al. 2007). The objective is to have a modeling system capable of assimilating SWOT data toward a near-real-time global estimation of water discharge.

HyMAP is inspired by the Catchment-based Macroscale Floodplain (CaMa-Flood) model (Yamazaki et al. 2011) and ISBA–Total Runoff Integrating Pathways (TRIP; Decharme et al. 2012) global flow routing schemes in that it simulates the horizontal water fluxes over continental surfaces where the runoff and baseflow (in this study, baseflow represents the vertical flux from unsaturated soil layer to saturated layer) generated by an LSM are routed through a prescribed river network to oceans or inland seas. The model simulates water level, discharge, and storage in rivers and floodplains at the daily time step with internal computational time steps that can be adjusted between a few minutes to several hours. The model is composed of four modules accounting for 1) the surface runoff and groundwater baseflow time delays, 2) a river–floodplain interface, 3) flow routing in river channels and floodplains, and 4) evaporation from open water surfaces. The main advances in the representation of physical processes in comparison to the previous two models are the introduction of time delays for both runoff and baseflow (section 2a), a floodplain elevation profile accounting for the representation of river surfaces (section 2b), the flow routing within the floodplain (section 2c), and the computation of surface water evaporation in offline LSM–FRS systems (section 2d). Also, HyMAP combines a relatively high spatial resolution of 0.25° with spatially distributed parameters. Figure 1 presents a schematic with the main variables of the model.

The runoff and baseflow generated by an LSM pass through the surface water or groundwater linear reservoirs, respectively, and then are routed using a kinematic wave formulation through a prescribed river network to oceans or inland seas. The river network is represented by a river channel reservoir and a floodplain reservoir in each grid cell. Similar to CaMa–Flood, river channel and floodplain are treated as continuous reservoirs in that water spilling from the river channel is stored in the floodplain. At each time step, the inflow water is redistributed between the river channel and floodplain reservoirs following stage–volume relationships derived from the topography of each grid cell. The outflow is then calculated independently for both floodplain and river considering different water depths and roughness coefficients.

Lowland topography and river network characteristics such as river length and slope are prescribed on

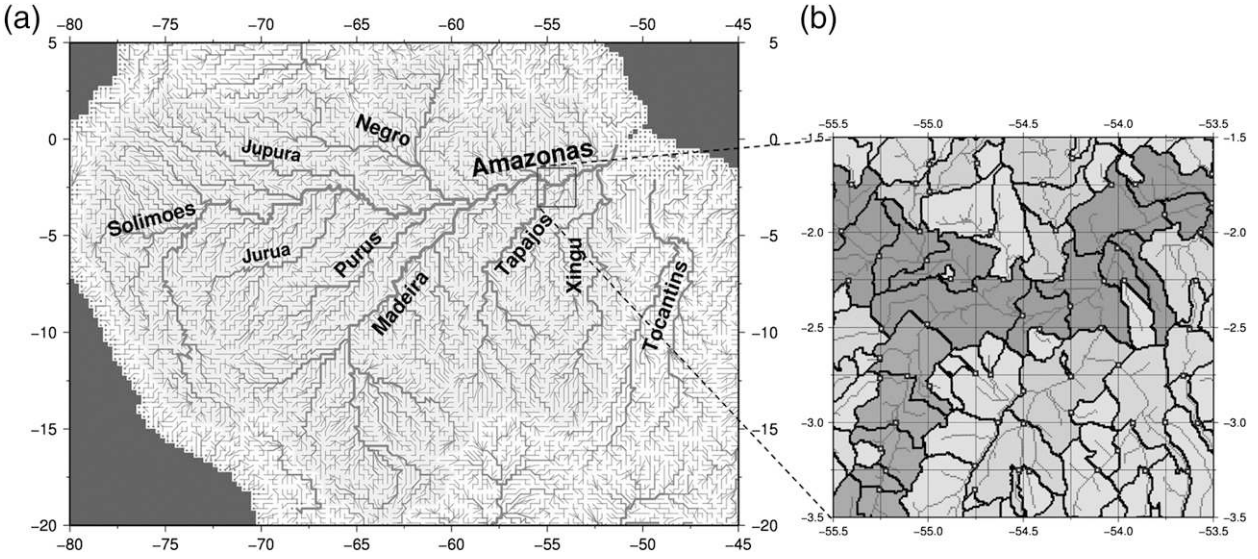

FIG. 2. Products of the upscaling procedure using the FLOW algorithm: (a) the river network map for the Amazon River and (b) subgrid topographic parameters. In (b), small squares represent outlet pixels, thick gray lines indicate river channel pixels, and black lines indicate the unit catchment attributed to each grid cell. Gray tones distinguish unit catchments of main river reaches and other tributaries.

a subgrid-scale basis according to the Flexible Location of Waterways (FLOW) method (Yamazaki et al. 2009). The fine-resolution flow direction map is given by the 1-km-resolution Global Drainage Basin Database (GDBD; Masutomi et al. 2009). The upscaling procedures for delineating coarse-resolution drainage areas and for extracting other river network parameters—such as flow directions, river length, and slope from GDBD—are described in Yamazaki et al. (2011). Figure 2 shows the river network map for the Amazon River and a snapshot of the subgrid data processing as prescribed by FLOW.

River width and bankfull height are derived from empirical relationships, which are functions of the average discharge. Water flow among grid cells is computed for both rivers and floodplains using the kinematic wave equation. Floodplain slope is the same as river's for simplicity. Manning's coefficients are spatially distributed according to river geometry and global land cover types.

Decharme et al. (2012), using ISBA–TRIP in online mode, have demonstrated that the evaporation from floodplains are essential to better estimate the water balance in arid regions subjected to monsoon regimes, such as the Parana and Niger River basins. The authors showed that considering floodplains can significantly increase the evapotranspiration, thereby decreasing the mean discharge in such regions, which was shown to improve results. The calculation of evaporation from open waters in offline mode can be performed in flow routing schemes if physical relationships between water surface and atmosphere are simplified. A Penman–Monteith formula is used in HyMAP to compute the evaporation from open waters. The next sections give a detailed description of the model features.

a. Module 1: The runoff and baseflow time delays

The concentration time (or time delay factor) is a physically based process representing the subgrid-scale routing. For each grid cell, both surface runoff I_s [mm $(\Delta t)^{-1}$] and baseflow I_b [mm $(\Delta t)^{-1}$] derived from an LSM pass through separate linear reservoirs with appropriate time delay factors. These values can vary from a few hours to several days, depending on hydrogeological characteristics of the catchment. The linear reservoir outflows can be represented by the following equation:

$$O_{s,b} = \frac{V_{s,b}}{T_{s,b}}, \tag{1}$$

where the subscripts s and b represent surface runoff and baseflow variables, respectively. The quantity $O_{s,b}$ [mm $(\Delta t)^{-1}$] stands for the outflow at time step t, $V_{s,b}$ (mm) the water stored in the linear reservoir, and $T_{s,b}$ the concentration time of the grid cell. The V is updated twice at each time step: at the beginning, adding the inflow $I_{s,b}$, and at the end, subtracting $O_{s,b}$.

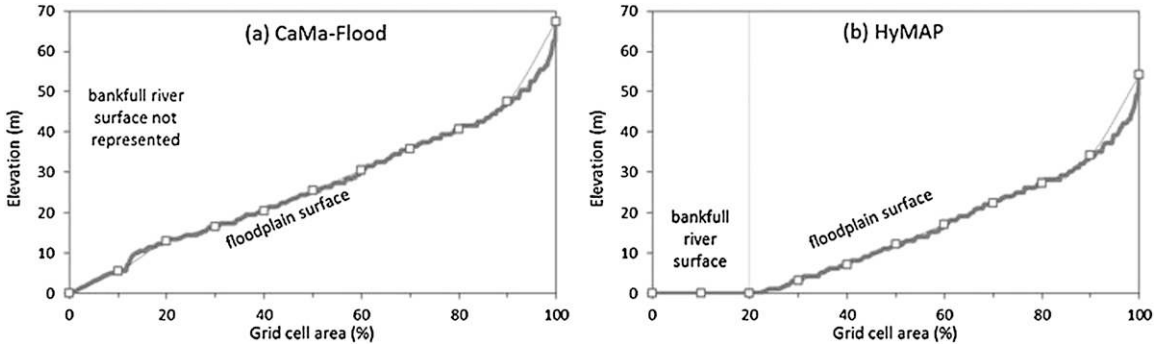

FIG. 3. Floodplain elevation profile represented in (a) CaMa–Flood (Yamazaki et al. 2011) and (b) HyMAP.

The baseflow time delay factor T_b is assumed to be spatially uniform and constant in time. The current parameterization of HyMAP coupled with ISBA defines $T_b = 45$ days. This value can be changed when other LSMs are used to force the flow routing scheme. The quantity T_s is computed for each grid cell from Kirpich (1940):

$$T_{s_j} = 3600\left(0.868\frac{\Delta x_j^3}{\Delta h_j}\right)^{0.385}, \qquad (2)$$

where Δx_j (km) is the distance between the farthest point within a grid cell and its outlet, and Δh_j (m) is the difference between the maximum and minimum elevations of the pathway. Both Δx_j and Δh_j are derived from the high-resolution DEM. At a 0.25° resolution, T_s values are quite low in comparison with T_b, varying from several minutes to a few days. Finally, the total discharge produced in each grid cell Q_c [m^3 $(\Delta t)^{-1}$] is computed as

$$Q_c = (O_s + O_b)A_c, \qquad (3)$$

where A_c stands for the gridcell area.

b. Module 2: The river–floodplain interface

The numerical representation of river channels and floodplains are similar to that in CaMa–Flood (Yamazaki et al. 2011) and ISBA–TRIP (Decharme et al. 2012). The river channel reservoir of a grid cell is defined using three parameters: channel length L (m); channel width W (m); and bank height H (m). If the actual water height in the river channel h_r (m) is higher than H, water is exchanged between river and floodplain reservoirs. This process is considered instantaneous at each time step so that water surface elevations of the river channel and the floodplain are the same.

A floodplain reservoir has a parameter for the unit catchment area A_c and a floodplain elevation profile, $h_f = f(A_f)$. The topographic parameters used to create the elevation profile are derived from the 30 arc-second Shuttle Radar Topography Mission (SRTM30) DEM processed with the FLOW method (Yamazaki et al. 2009). The errors of SRTM30 DEM due to the limitations of satellite radar sensing (e.g., vegetation canopies, subpixel-sized structures, and random radar speckle) are removed as much as possible before applying the FLOW algorithm for deriving the topographic parameters. The method applied for SRTM30 error correction is summarized in Yamazaki et al. (2012).

Some examples of floodplain elevation profile suggested by Decharme et al. (2012) and Yamazaki et al. (2011) consider that all of the surface area within a grid cell can be potentially flooded, neglecting the existence of the river surface (Fig. 3a). Indeed, it is a difficult task to define reliable river surfaces globally since river geometry is generally defined using statistical relationships: no global land cover dataset with sufficient spatial resolution is currently available to derive precise river widths. In this sense, a simple solution is suggested in this study. First, the bankfull river surface is defined as the product between the river length derived from the DEM processing and the river width obtained from an empirical equation (see below). Also, it is assumed that rivers are always composed by the lowest subgrid pixels within a grid cell. Then, the elevation of the highest "river pixel" is subtracted from the elevation profile (Fig. 3b). In this sense, for any river water storage more than zero, the grid cell will have a minimum water surface corresponding to the river surface area.

The river channel and floodplain water exchanges at each time step are represented as follows:

$$\text{if} \quad S_{r_{\max}} \le S, \quad \begin{aligned} S_r &= S \\ h_r &= S_r/(W \times L) \\ S_f &= 0 \\ h_f &= 0 \\ A_f &= 0, \end{aligned} \qquad \text{and} \qquad (4)$$

$$\text{if} \quad S_{r_{\max}} > S, \quad \begin{aligned} S_r &= S - S_f \\ h_r &= S_r/(W \times L) \\ S_f &= \int_0^{A_f} [h_f - h(A_f)]\, dA \\ h_f &= h_r - H \\ A_f &= h^{-1}(h_f), \end{aligned} \tag{5}$$

where subscripts r and f represent river channel and floodplain variables, respectively. The quantity S (m^3) stands for the total water storage in the grid cell, S_r (m^3) and S_f (m^3) the river channel and floodplain water storages, h_r (m) and h_f (m) water depths, W (m) the river width, L (m) the river length, and A_f (m^2) the flooded area. The $S_{r_{\max}}$ (m^3) stands for the river bankfull water storage, and is given as $S_{r_{\max}} = H \times W \times L$, where H (m) is the river bankfull height.

The temporal change of water storage in river channels and floodplains of a grid cell S is defined by the continuity Eq. (6) considering linear reservoir outputs, river and floodplain discharges to the downstream grid point, river and floodplain discharges from the upstream grid points, and evaporation from the floodplains:

$$S^t = S^{t-1} + \left[Qc^{t-1} + \sum_{k=1}^{\text{nUp}} (Q_{r,k}^{t-1} + Q_{f,k}^{t-1}) - Q_r^{t-1} - Q_f^{t-1} - E^{t-1} \right] dt, \tag{6}$$

where t is time, and dt represents the time step. The index k stands for the nUp upstream grid cells of the target grid point.

c. *Module 3: Flow routing in river channels and floodplains*

Water discharge in both the river and the floodplain is calculated by the kinematic wave equation. Using the Manning formula for a rectangular cross section and large width-to-depth ratio, water discharge in the river channel Q_r ($m^3\ s^{-1}$) can be defined as

$$Q_r = \frac{1}{n_r} i_r W_r h_r^{5/3}, \tag{7}$$

where n_r is the roughness coefficient for rivers; i_r is a constant riverbed slope derived from topographic information and corresponds to the slope between the target and downstream grid cells.

Similarly, water discharge in the floodplains Q_f ($m^3\ s^{-1}$) is given as

$$Q_f = As_f v_f = \overline{w}_f \overline{h}_f v_f, \tag{8}$$

where As_f (m^2) is the floodplain cross-sectional area, v_f (m s^{-1}) the mean flow velocity through the floodplain section, and w_f (m) and h_f (m) stand for the mean width and depth of the floodplains, respectively, which are computed as follows:

$$\overline{w}_f = \frac{A_f}{L} \quad \text{and} \tag{9}$$

$$\overline{h}_f = \frac{S_f}{L\overline{w}_f} = \frac{S_f}{A_f}. \tag{10}$$

The quantity v_f can be defined by using Eqs. (8) and (9) in the Manning formula:

$$v_f = n_f^{-1}(i_f^{1/2}) \left(\frac{S_f}{A_f} \right)^{2/3}, \tag{11}$$

where n_f is the Manning roughness coefficient for floodplains that varies according to the vegetation type (see below) and, for simplicity, i_f is considered equal to i_r.

Finally, combining Eqs. (7) and (10) yields

$$Q_f = \frac{1}{n_f} i_f \frac{S_f^{5/3}}{L A_f^{2/3}}. \tag{12}$$

1) River width and depth

Although flow routing schemes are very sensitive to the accuracy of river geometry, these data are very scarce on the global scale. In this sense, empirical methods are normally employed to determine river width and depth spatially. These methods can be functions of hydrological or geomorphological characteristics (e.g., drainage area and water discharge) and have been largely used in the literature for large-scale hydrological modeling (e.g., Arora and Boer 2001; Coe et al. 2008; Decharme et al. 2012; Yamazaki et al. 2011). In HyMAP, river width is defined for each grid cell based on an empirical relationship between W and the mean annual discharge:

$$W = \max(10, \beta \times Q_{\text{med}}^{0.5}), \tag{13}$$

where Q_{med} ($m^3\ s^{-1}$) is the annual mean discharge in each grid cell estimated using the global runoff database from Cogley (2003). As suggested by Decharme et al. (2012), β is defined for five different hydrological regions of the world (see Fig. 4). For equatorial or subtropical basins, which include the Amazon basin, $\beta = 18$. The H is computed via a linear relationship with W:

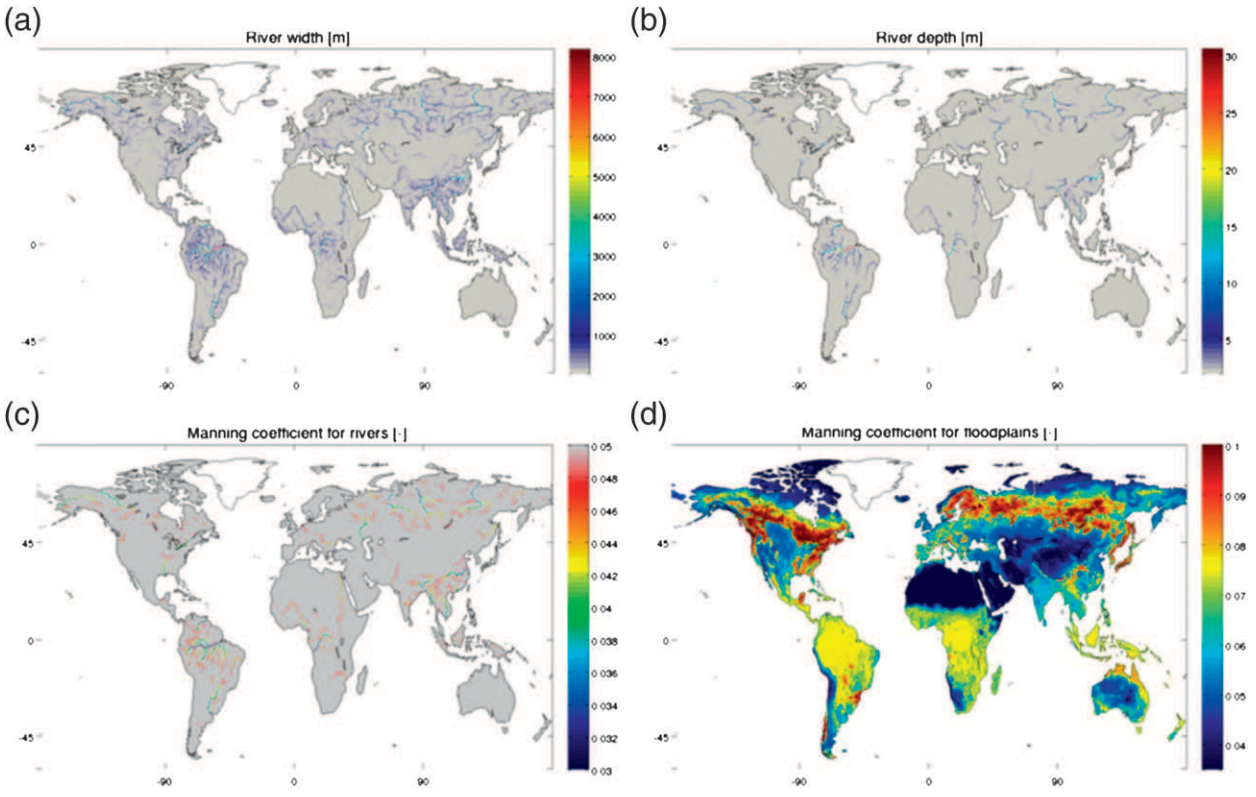

FIG. 4. Global distribution of HyMAP parameters at a 0.25° spatial resolution: (a) river width derived from Eq. (13); (b) river depth derived from Eq. (14); (c) Manning roughness coefficient for rivers, as described by Eq. (15); and (d) Manning roughness coefficient for floodplains, Eq. (16).

$$H = \max(2.0, \alpha \times W) \quad \alpha = 3.73 \times 10^{-3}. \tag{14}$$

2) MANNING COEFFICIENT FOR RIVER CHANNELS AND FLOODPLAINS

The Manning roughness coefficient n is an empirical parameter and general values can be prescribed for most types of channels and surfaces. For practical reasons, in many studies, n is considered constant for the whole domain, with values of about $n = 0.03$ for open channels. HyMAP considers the spatial variability of n in both rivers and floodplains as functions of land cover and water depth. In this study, the Manning coefficient of river channels n_r varies according the following formula:

$$n_r = n_{\min} + (n_{\max} - n_{\min})\left(\frac{H_{\max} - h}{H_{\max} - H_{\min}}\right)^{1/3}$$
$$n_{\min} = 0.03 \quad n_{\max} = 0.05, \tag{15}$$

where $n_{\max}$ and $n_{\min}$ are the maximum and the minimum values of the Manning coefficient selected from values suggested in the literature (Chow 1959) and $H_{\max}$ and $H_{\min}$ the maximum and minimum river depths as provided by Eq. (9).

The Manning coefficient for floodplains n_f is spatially distributed as a function of 12 land cover types at 0.25° resolution derived from the 1-km ECOCLIMAP dataset (Masson et al. 2003). The n_f values are larger in tropical forests and lower for bare soils and rocks. The 12 vegetation types are described in Table 1. A similar solution, as suggested by Decharme et al. (2012), is used:

$$n_f = \sum_{k=1}^{12} (\mathrm{lcov}_i \times n_{f_i}), \tag{16}$$

where lcov_i stands for the gridcell fraction of each vegetation type i listed in Table 1 and n_{f_i} the respective Manning roughness coefficient for floodplains. Figure 4 shows the global distribution of both n_r and n_f. Manning values for floodplains have also been determined based on previous studies found in the literature.

d. Module 4: Evaporation from floodplains

A simple approach is used to estimate the evaporation from the open waters E_w ($\mathrm{m^3\ day^{-1}}$). First, the potential evaporation E ($\mathrm{mm\ day^{-1}}$) is calculated by the Penman–Monteith equation once a day, by setting the surface resistance to zero:

TABLE 1. Land cover types and respective Manning roughness coefficients for floodplains n_f. The land cover classification is specified by the 1-km ECOCLIMAP dataset (Masson et al. 2003).

	Land cover types	Manning roughness coefficient
1	Flat bare soil	0.035
2	Rocks	0.035
3	Permanent snow and ice	0.035
4	Tropical forest	0.075
5	Coniferous forest	0.100
6	Broadleaf evergreen forest	0.100
7	C3 crops	0.050
8	C4 crops	0.050
9	Irrigated crops	0.050
10	Grassland	0.050
11	Tropical grassland	0.075
12	Park mashes	0.075

$$E = \left(\frac{\Delta \times A + \rho_A \times c_p \times \dfrac{D}{r_a}}{\Delta + \gamma} \right) \times \frac{M}{\lambda \times \rho_W}, \quad (17)$$

where Δ (kPa $^\circ C^{-1}$) is the gradient of the saturated vapor pressure–temperature function; A (MJ m^{-2} s^{-1}) is the available energy; ρ_A (kg m^{-3}) and ρ_W (kg m^{-3}) are the specific mass of air and water, respectively; c_p is the specific heat of moist air (MJ kg^{-1} $^\circ C^{-1}$); D (kPa) is the vapor pressure deficit; γ (kPa $^\circ C^{-1}$) is the psychrometric constant; r_a (s m^{-1}) is the aerodynamic resistance; λ (MJ kg^{-1}) is the latent heat of vaporization; and M is a time step unit conversion from m s^{-1} to mm Δt^{-1}. Available energy and aerodynamic resistance can be calculated following Shuttleworth (1993). For simplification purposes, water albedo and emissivity were fixed as 0.07 and 1, respectively.

Then, the real or actual evapotranspiration rate ET (mm day^{-1}) diagnosed by the LSM, is subtracted from E and the result is multiplied by the water surface A_f, resulting in the effective evaporation from open waters:

$$E_w = \max[0, (E - \mathrm{ET})A_f]. \quad (18)$$

The computation is done once per day using standard input meteorological forcing variables and assuming that the water in the floodplains and river have the same temperature as the air (a predicted or prescribed surface water temperature is not needed). This is consistent with the neglect of stability corrections in the Penman–Monteith equation (using the daily time step).

3. Experimental design

HyMAP was run over the Amazon basin at the 0.25° spatial resolution during the 1986–2006 period. The model time step was set as 15 min and outputs provided as daily averages. Daily surface runoff and baseflow derived from ISBA are used as inputs in HyMAP. Meteorological forcings and the total evapotranspiration calculated by ISBA are also needed to estimate the remaining energy available for the evaporation from open waters. Since the coupling is performed in offline mode, there is no feedback from HyMAP to ISBA, which implies that floodplains do not cause reinfiltration into the LSM or influence the soil moisture. Main land surface parameters used by ISBA—such as land cover, vegetation parameters, soil textural properties, and topography—are not discussed (a full description can be found in Decharme et al. 2012).

a. Meteorological forcings

The meteorological dataset used as forcing for ISBA is provided by Princeton University on a 3-hourly time step and at a 1° resolution (Sheffield et al. 2006). This dataset is based on the National Centers for Environmental Prediction–National Center for Atmospheric Research (NCEP–NCAR) reanalysis. Sheffield et al. (2006) carried out corrections of the systematic biases in the 6-hourly NCEP–NCAR reanalyses via hybridization with global monthly gridded observations. In addition, the precipitation was disaggregated in both space and time at 1° resolution via statistical downscaling and at 3-hourly time step using information from the 3-hourly Tropical Rainfall Measuring Mission (TRMM) dataset. The 3-hourly precipitation from Sheffield et al. (2006) are then hybridized to match the monthly value from the Global Precipitation Climatology Center (GPCC) Full Data Product V4, as proposed in Decharme et al. (2012).

b. Evaluation dataset

1) IN SITU OBSERVATIONS

Daily observed water discharge data at 172 gauging stations operated by the Brazilian Water Agency (ANA) are used to evaluate HyMAP streamflows. These gauging stations have time series with at least one year of observations within the 1986–2006 period. Observed water discharge at both Jatuarana and Careiro stations, located along the Amazon River, can be summed providing the water discharge downstream Negro River's confluence. The ''new station'' is called Jatuarana+Careiro or station 2.

Observed flow velocities (v) at 153 gauging stations with areas bigger than 15 000 km^2 are also considered in the evaluation procedure. These data are also maintained by ANA and acquired only a few times per year in order to calibrate rating curves. Available v values are averages of numerous instantaneous and quasi-instantaneous

measurements, which are, in most cases, obtained by acoustic Doppler current profiler (ADCP) or Pygmy meter measurements within the river cross section. The selected gauging stations have between 5 and 151 daily flow velocity observations within the 1986–2006 period, totaling 9149 observations. Drainage areas of both water discharge and flow velocity gauging stations range from 1000 to 4 670 000 km^2. Errors of in situ data are generally on the order of 10%–15% and can be mainly caused by imperfect samplings at actual cross sections with considerable velocity gradients.

2) RADAR ALTIMETRY DATA

Data provided by the altimeter on board the *Envisat* satellite are considered in this study. *Envisat* orbits on a 35-day temporal resolution (duration of the orbital cycle) from latitude 81.5°N to 81.5°S, and 70-km intertrack spacing at the equator. The ranges used in this study are those issued by the ICE-1 algorithm (Bamber 1994). Errors in altimetric time series along rivers within the Amazon basin are in the order of tens of centimeters. *Envisat* data are freely available on the Hydroweb server (http://ctoh.legos.obs-mip.fr/products/hydroweb) (Crétaux et al. 2011). Altimetric data at 294 virtual stations (VS) located within Amazon basin are considered in this study. Selected VS cover most Amazon River's tributaries and other small rivers, with drainage areas ranging from 10 000 to 5 238 800 km^2. Time series vary from 34 to 41 altimetric observations for the 2002–06 period.

3) FLOODPLAIN EXTENT FROM MULTISATELLITE TECHNIQUE

Floodplains simulated by HyMAP were evaluated against the multisatellite estimates of surface water extent from Papa et al. (2010). This dataset, called P10 hereafter, is available at a monthly time step for 1993–2004, with a spatial resolution of 773 km^2 (i.e., equal-area grid of 0.25° × 0.25° at the equator). It was generated from a complementary multiple satellite observations, including passive [Special Sensor Microwave Imager (SSM/I)] and active [European Remote Sensing (ERS) series satellites] microwaves, along with visible and near-infrared imagery [Advanced Very High Resolution Radiometer (AVHRR)].

Because the dataset makes no distinction between floodplains and other kinds of surface water bodies—including lakes, anthropogenic and natural reservoirs, or irrigated agriculture—Decharme et al. (2012) show that a hybrid version of P10 is more suitable to be directly compared with the simulated floodplain extents derived from flow routing schemes such as HyMAP or ISBA–TRIP. Following a similar approach, the Global Lakes and Wetland Database (GLWD) and the Monthly Irrigated and Rainfed Crop Areas (MIRCA2000) products were used to build an alternative product to P10 that is more comparable with model simulations. The GLWD data (Lehner and Döll 2004) gives the global distribution of 12 types of surface water bodies, including lakes, wetland, and floodplains at 30-arc-second resolution (~1 km at the equator), and the MIRCA2000 product (Portmann et al. 2010) provides the classification of 26 irrigated crops for each month of a year around the year 2000 at 5-arc-minute resolution (~9.2 km at the equator). In this study, both products are resized to fit the 0.25° model grid. Decharme et al. (2012)'s technique consists of subtracting the GLWD lakes and bogs, fen, and mire areas (LGLWD), as well as the MIRCA2000 annual cycle I_{mth}, from P10 where the GLWD rivers, floodplains, and intermittent lake/floodplain areas (FGLWD) exist:

$$\mathrm{FLD}_{\mathrm{obs}}(t) = \delta \times \max[0, \mathrm{P10}(t) - L_{\mathrm{GLWD}} - I_{\mathrm{mth}}] \,\Big|\, \begin{matrix} \delta = 1 & \forall & F_{\mathrm{GLWD}} > 0 \\ \delta = 0 & \forall & F_{\mathrm{GLWD}} = 0 \end{matrix}, \tag{19}$$

where $\mathrm{FLD}_{\mathrm{obs}}$ stands for the new final product and t the time step in months.

4. Results and discussion

a. Evaluation of water discharges

About 50% of the stations have drainage areas bigger than 30 000 km^2. This large dataset provides the unique opportunity for thoroughly evaluating a flow routing scheme over the Amazon basin. Based on observations at eight stations (gauging stations 1, 2, 3, 4, 7, 9, 11, and 13), one can notice in Fig. 5 a changing water discharge regime along the Solimões–Amazon main stream. In the upper part of the Solimões River, a large gradient (resulting owing to the relatively close proximity to the Andes) causes the noisy annual cycles with abrupt changes, as seen at stations 13 (Tabatinga), 11 (Teresina), 9 (São Paulo de Olivença), and 7 (Santo Antonio do Içá). In the lower part, high and smooth water discharges at stations 4 (Itapeua), 3 (Manacapuru), 2 (Jatuarana+Careiro), and 1 (Óbidos) are a result of both the diffusive effect of a low gradient in lowlands and water storage in floodplains and

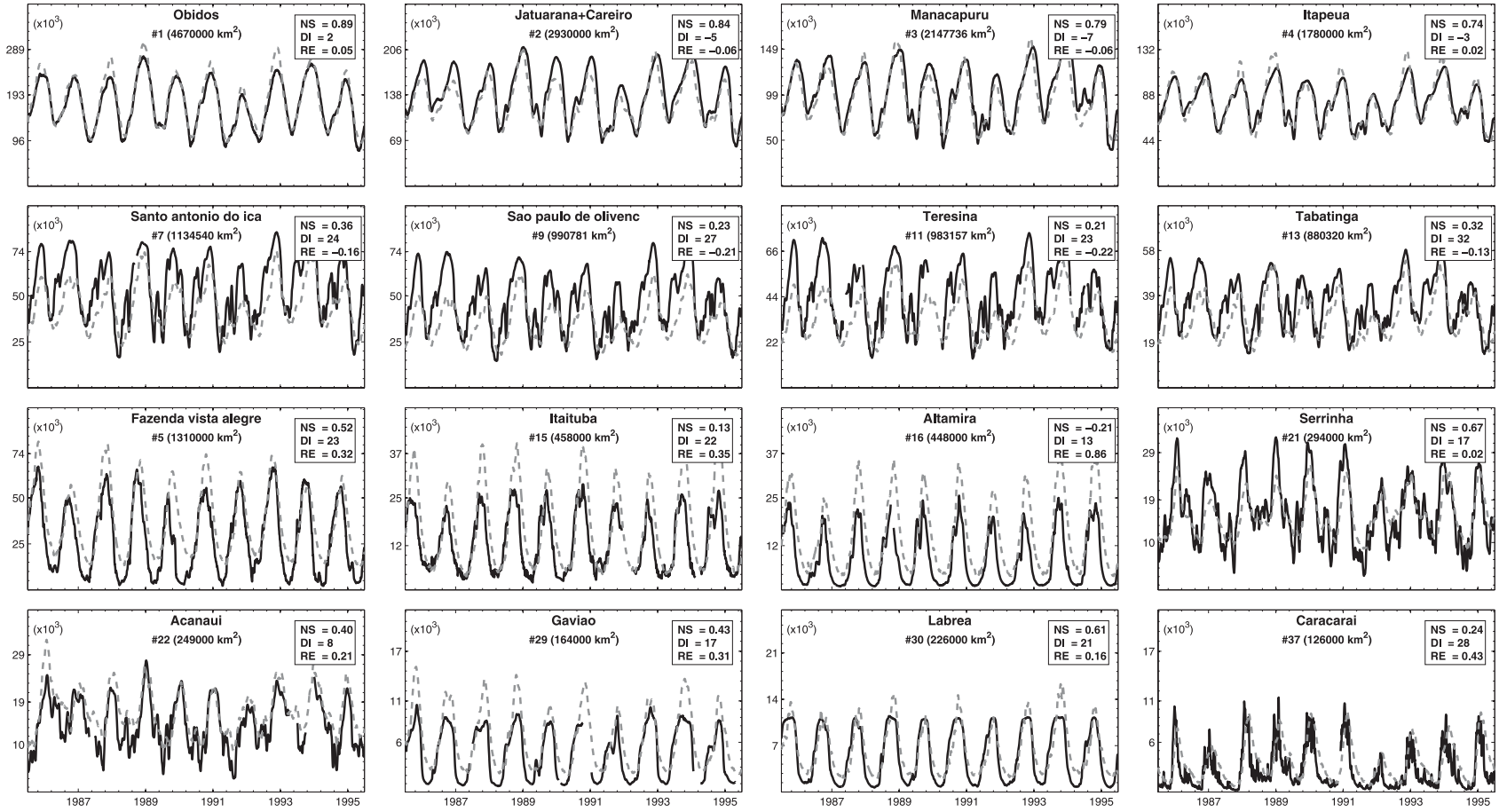

FIG. 5. Hydrographs at 16 gauging stations. Drainage areas and performance coefficients for daily water discharge (NS, DI, and RE) are also provided for selected stations. Values of DI are in days. Model outputs are in dashed gray lines and in situ observations in black. Water discharge units are in 10^3 m^3 s^{-1}. The locations of selected stations are indicated in Fig. 7.

the massive contribution of important tributaries such as the Purus, Madeira, and Negro Rivers.

Daily water discharges have been quantitatively evaluated by means of three performance coefficients: the delay index (DI) (days), the Nash–Sutcliffe coefficient (NS), and the volume error of streamflows (DV). The delay index (DI) (days) is used to measure errors related to time delay between simulated and observed hydrographs. The DI is computed using the cross-correlation function Rxy (m) from simulated (x) and observed (y) time series, where DI equals the value of the time lag m where Rxy (m) is maximum (Paiva et al. 2012). The quantities NS and DV are represented by the following equations:

$$\mathrm{NS} = 1 - \frac{\sum_{t=1}^{\mathrm{nt}} (y_t - x_t)^2}{\sum_{t=1}^{\mathrm{nt}} (y_t - \overline{y})^2} \quad \text{and} \tag{20}$$

$$\mathrm{DV} = \frac{\sum_{t=1}^{\mathrm{nt}} x_t - \sum_{t=1}^{\mathrm{nt}} y_t}{\sum_{t=1}^{\mathrm{nt}} y_t}, \tag{21}$$

where t is the time step; nt the total number of days with observed data; x and y are, respectively, the simulated and target (observed) signals at time step t; and $\overline{y}$ is the mean value of the target signals for the entire period. The NS ranges from $-\infty$ to 1, where 1 is the optimal case and 0 is when simulations represent observed signals as well as the mean value. One can obtain RE values in percentage by multiplying by 100.

Results show that HyMAP can satisfactorily reproduce water discharges along the Solimões–Amazon main stream, representing well the aforementioned discharge characteristics. At Óbidos, the gauging station representing most of the Amazon basin outflow, located about 800 km upstream from the river mouth, discharges are very well simulated with NS = 0.89. This result shows improvements in comparison with previous daily water discharge simulations at Óbidos, where NS values reached 0.78 and 0.83 with kinematic and diffusive wave equations, respectively (Yamazaki et al. 2011). Simulations with ISBA–TRIP resulted in NS values of 0.69 in offline mode (i.e., without floodplains) and 0.83 in online mode (i.e., with floodplains accounting for soil moisture and evaporation from open waters). The slightly improved performance with this model can be partially explained by the fact that both of the aforementioned models are simpler than HyMAP with respect to the horizontal water flow parameterization such as a limited representation of physical processes, global-scale parameter estimation, and, in the case of ISBA–TRIP, coarser spatial resolution. Simulated wave peaks are in phase with observations with a mean delay of only two days (DI = 2). Mean simulated water discharge overestimates the observations by about 5%. This error is easily perceptible during peaks and can be mainly attributed to forcing uncertainties over the basin. HyMAP also performed very well at stations 2, 3, and 4, all of which are located along the lower Solimões–Amazon main stream, with NS values varying from 0.74 to 0.84 and relative errors (RE) from −6% to 2%. On average, simulated discharge peaks occur 3–7 days before observations at these stations. Except for station 2, all of these gauging stations experience slightly overestimated peaks, as shown in Fig. 5.

Simulated discharges at gauging stations 7, 9, 11, and 13 have NS coefficients between 0.21 (station 13) and 0.36 (station 7). Simulations represent well dry seasons but underestimate peaks systematically, resulting in negative volume errors RE ranging from −13% (station 13) to −22% (station 11). Overall, HyMAP has very good discharge simulations at the basinwide scale. Better results are obtained in larger rivers while smaller tributaries had medium or poor performances. This is expected and fairly typical of such large-scale models since the precipitation and basin parameter errors are larger at small scales. As shown in Fig. 6, among all stream gauges used in the evaluation process, 39 (or 23% of the total) have NS higher than 0.50 and 117 (or 68%) have values above zero. About 28% of the stations have volume errors lower than 15% and they are located mostly in the western and central parts of the basin. As shown in Fig. 7, the overestimated mean discharges in most rivers draining over the southern part of the basin are probably a result of errors in the forcings. For instance, the mean discharges in the Madeira River are overestimated in about 32% at Fazenda Vista Alegre (station 5). Similar results are obtained for the Purus (RE = 32% at Gavião—station 29), Tapajós (RE = 35% at Itaituba—station 15), and Xingu (RE = 82% at Altamira—station 16). At these same stations, DI values are of 23, 22, and 13 days, respectively, and NS values of 0.43, 0.13, and −0.21. Good results are obtained for the Negro River at Serrinha (station 21), with NS = 0.67, DI = 2 days, and RE = 2%. High delay indexes can be explained by both the use of a single T_b value for the whole basin and the kinematic wave assumption in flat water surfaces.

b. *Evaluation of water levels*

The water level evaluation at 294 *Envisat* virtual stations gives a wide overview of model performance at the basin scale. Three performance coefficients have been used to evaluate simulated water levels: the correlation

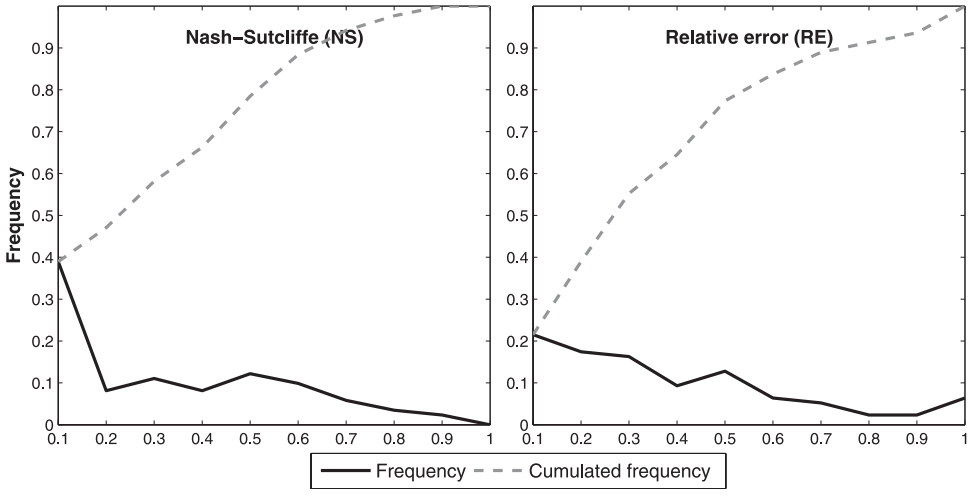

FIG. 6. The histogram of the normalized frequency of (left) the Nash–Sutcliffe coefficient (NS) and (right) absolute values of relative error (RE) of daily water discharges at 172 gauging stations. The range is from 0 to 1 with a bin size of 0.1. The best overall simulations are skewed the most to the right. Negative NS values are included in values between zero and 0.1.

coefficient (r), the tangent derived from a linear regression between simulated and observed signals (α), and the NS coefficient of unbiased water levels (NSA). The quantity NSA is defined as follows:

$$\mathrm{NSA} = 1 - \frac{\sum_{t=1}^{\mathrm{nt}} [(y_t - \overline{y}) - (x_t - \overline{x})]^2}{\sum_{t=1}^{\mathrm{nt}} (y_t - \overline{y})^2}, \qquad (22)$$

where $\overline{x}$ stands for the mean value of the simulated signals for the entire period. Similarly to NS, NSA ranges from $-\infty$ to 1, where 1 is the optimal case. The following correction has been applied to α:

$$\begin{matrix} \alpha & \text{if} & \alpha \le 1 \\ \alpha^{-1} & \text{if} & \alpha > 1 \end{matrix}. \qquad (23)$$

In this sense, the optimal α value is one and any other result below unity means that the amplitude of one of the signals is overestimated or underestimated.

As shown in Fig. 8, good correlations between simulated and observed water levels are found in most of the main rivers. This indicates that the model can properly represent the water level interannual variations. The averaged r of 18 VS along the central and low Solimões–Amazonas Rivers is 0.91, ranging from 0.83 (VS-36) to 0.96 (VS-24). These results present improvements in comparison to previous model evaluations with radar altimetry data over the Amazon River (Coe et al. 2008), where the averaged correlation between Ocean Topography Experiment (TOPEX)/Poseidon and water level simulations at eight VS along the same river reach is 0.70.

About 54% of VS have r values greater than or equal to 0.75 and 58% have NSA values higher than or equal to 0.50. Most of these stations are located over main rivers with large drainage areas. As shown in Fig. 8, virtual stations located in headwater catchments and on the western side of the basin, such as the Japurá River, the upper reaches of rivers draining the Andes and the lower Negro River, perform worse. The spatial distribution of coefficient a indicates that the amplitudes between simulated and observed water levels are in agreement in the Madeira and Branco Rivers and along the central Solimões and Negro Rivers. However, a significant discrepancy can be seen in other areas of the basin.

Water level errors in headwater catchments can be explained using arguments similar to those used for discharge error: mainly owing to meteorological forcing uncertainties at refined scales and simplified model physics. In other places, the degraded model performance (indicated by the low a coefficients) is also due to the application of a unique equation defining river geometry. Indeed, river width can have a great impact on water level amplitudes, as demonstrated in Getirana et al. (2012). In some specific cases, such as the lower Amazon River, low a values do not prevent the model from obtaining very good performances in terms of discharge. For example, even if the virtual station VS-10 had $a = 0.48$ (see Fig. 8), the simulated water discharge at Óbidos station (located a few kilometers away) resulted in NS = 0.89. The 1-month delay observed in the water discharge time series at the Caracaraí station is also evident in the simulated water levels at virtual

stations along the Branco River (e.g., VS-227). This indicates that the hydrological regime of this basin might be controlled by surface water rather than groundwater, implying that a high volume of baseflow stored in the baseflow reservoir can cause a significant flood wave delay.

c. *Evaluation of flow velocities*

Previous regional and global flow routing schemes compute flow velocity assuming a time-independent v parameterized as a function of one or more river physical characteristics, including slope and mean discharge (e.g., Vörösmarty et al. 1989; Miller et al. 1994; Sausen et al. 1994; Hagemann and Dümenil 1998). Other approaches have used traditional equations such as the Manning formula (e.g., Arora et al. 1999; Decharme et al. 2012; Yamazaki et al. 2011) and adaptations of the Chezy formula (e.g., Coe et al. 2008). These models simulate water flow only in river banks, while floodplains (if represented) are considered as static reservoirs. HyMAP calculates flow velocities in both rivers and floodplains by using Manning's formula with roughness coefficients adapted to the land cover type. Results show that flow velocities along the Solimões–Amazon main stream vary from 0.8 to 1.6 m s^{-1}, with lower values occurring between September and November and high values between March and May. These results are in agreement with other models based on similar formulations (e.g., Decharme et al. 2012; Yamazaki et al. 2011).

However, observations at gauging stations reveal that v values are higher than those given by the model. According to Fig. 9, simulated velocities are underestimated in large rivers, where the mean error e, computed as the ratio between mean simulated $\overline{v}_{\text{sim}}$ and observed $\overline{v}_{\text{obs}}$ flow velocities ($e = \overline{v}_{\text{sim}}/\overline{v}_{\text{obs}}$) is less than 1. In some regions, such as the southern Amazon basin, mean simulated v values are overestimated ($e > 1$). These differences are mainly due to (i) the simplified representation of river geometry and (ii) errors in the forcing data. Water depth h is the only time-dependent variable in the Manning's formula, while the roughness coefficient n and river slope i_r are constant. This means that changes in v is directly proportional to h. At each time step and grid cell, h is computed as a function of the river width W, length L, and water storage S_{riv} [Eqs. (4) and (5)]. Overestimated runoff and baseflow may result in higher water storage and, as a consequence, a higher h value. This explains the overestimation of both water discharge (RE > 0) and flow velocities ($e > 1$) at most gauging stations located in the southern Amazon basin (including Xingu, Tapajós, and Madeira River basins), as one can see in Fig. 9.

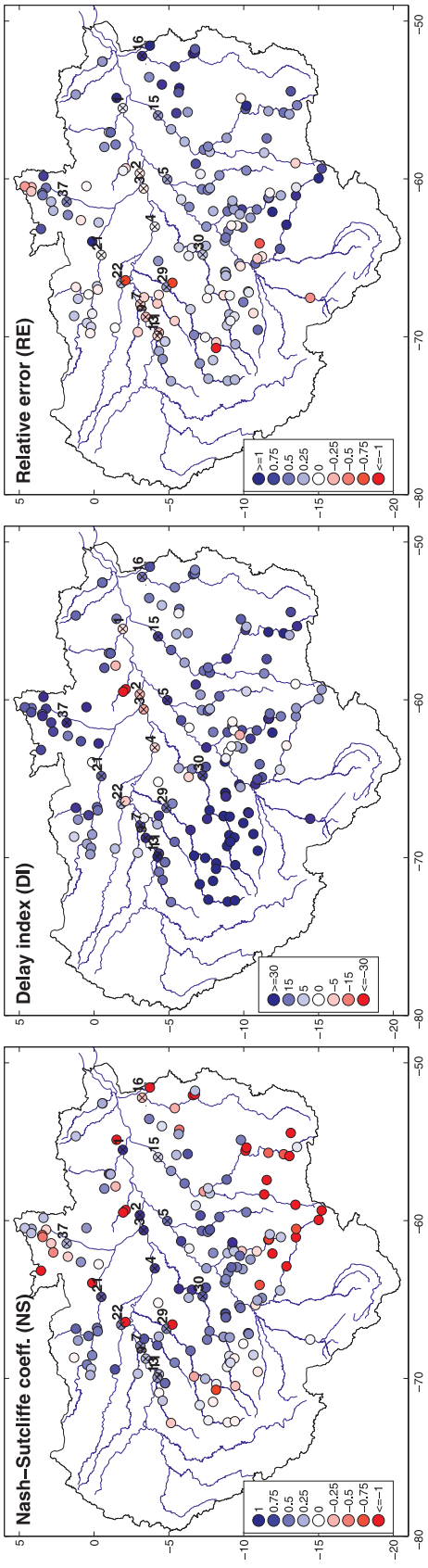

FIG. 7. Evaluation of simulated daily water discharge at 172 gauging stations within the Amazon basin. (left)–(right) Nash–Sutcliffe coefficient (NS), delay index (DI, in days), and relative error (RE).

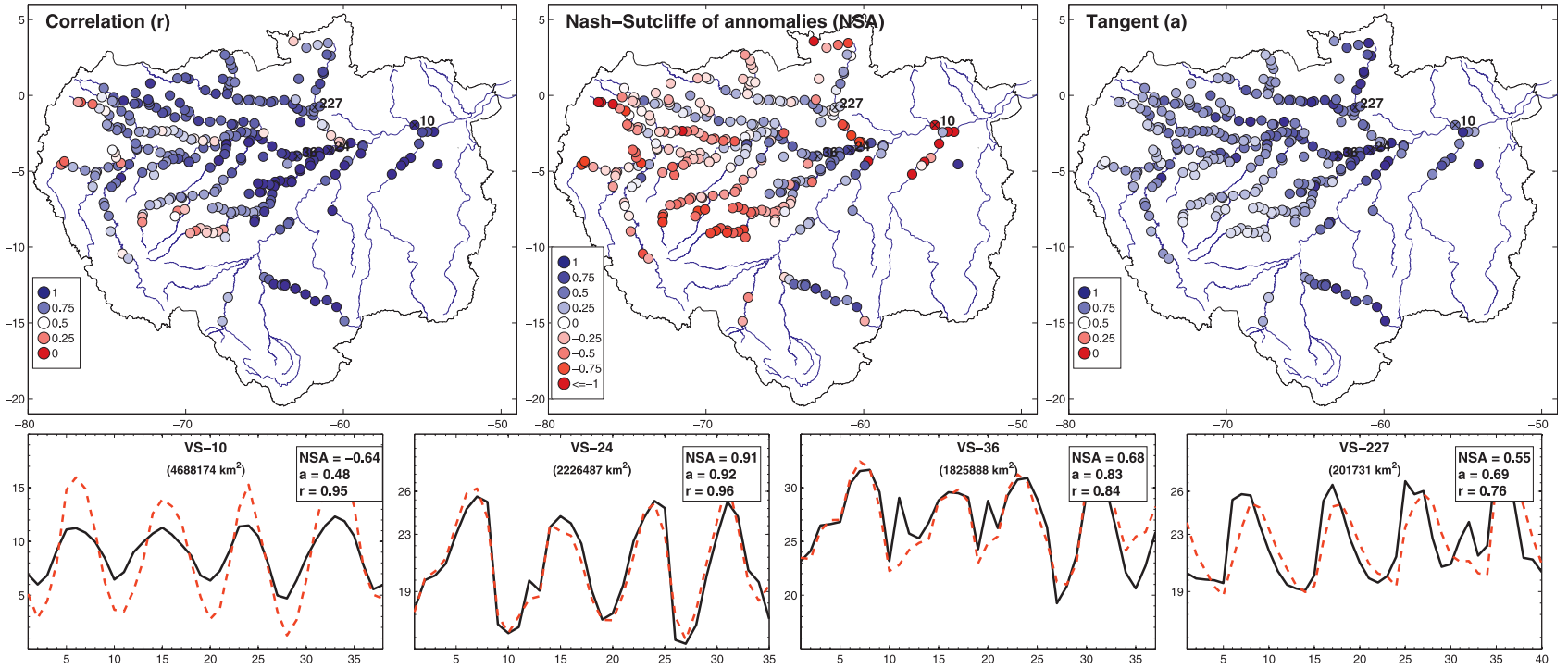

FIG. 8. Evaluation of simulated water levels against *Envisat* altimetric data. (top) Correlation (r), Nash–Sutcliffe coefficient of anomalies (NSA), and tangent (a) of simulated water levels at 294 virtual stations. (bottom) Water level time series at VS-10, VS-24, VS-36, and VS-227. Water level units are in meters and the abscissas in *Envisat* cycles available in the 2002–06 period. Model outputs are in dashed red lines and satellite observations in black.

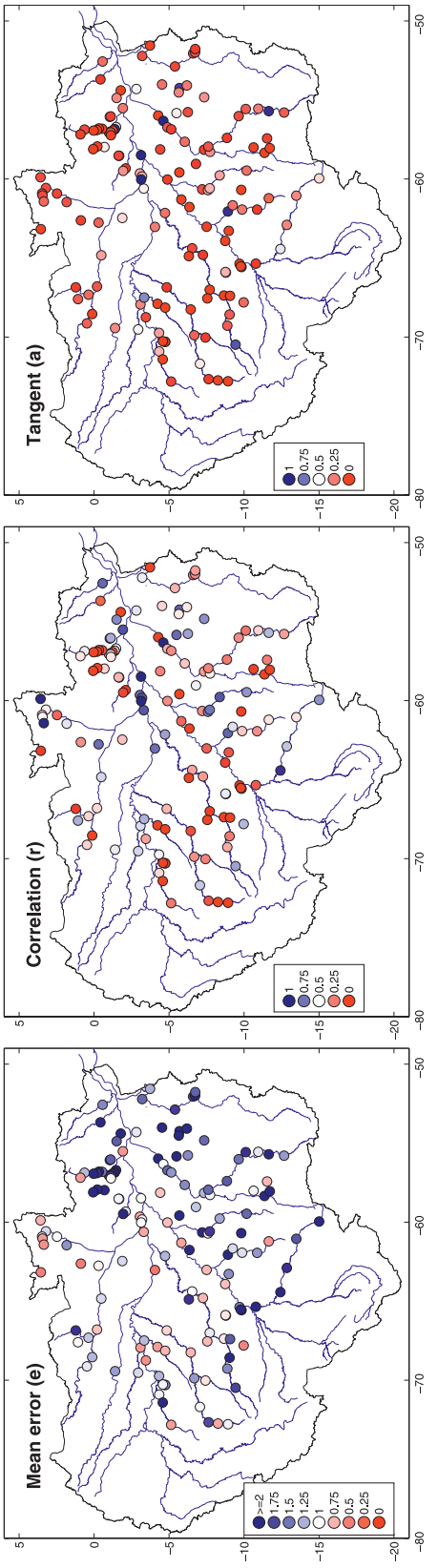

FIG. 9. Evaluation of simulated flow velocities at 153 gauging stations within the Amazon basin. (left)–(right) Mean error (*e*), correlation (*r*), and tangent (*a*).

d. Evaluation of floodplain extent

Figure 10 compares the spatial distribution of floodplains over the entire Amazonian basin from the model with the satellite-derived estimates for two distinct time periods: the dry (October 1995) and humid (June 1996) seasons. The simulated floodplain extent agrees with satellite-based estimates along the major river channels such as the Solimões, Amazon, Negro, Purus, and Madeira Rivers. However, differences are present in the Northern Negro and Branco River basins and southern Xingu River basin. Also, simulations show a very dispersed floodplain spatial distribution, which is not observed in the satellite-based estimates. These inconsistencies might be due to the model parameterizations and algorithms used to process satellite data, as discussed later in this section.

Note that the visual comparison of flooded areas is not straightforward because of the discrepancy between the satellite product's rectangular grid and the model's unit catchment (as shown in Fig. 2b). This means that, in some cases, a single unit catchment can represent surface areas corresponding to several satellite rectangular grid cells. This situation is most frequent in the main rivers, where large satellite-derived floodplain extents (e.g., Solimões–Amazon Rivers in the central Amazon area) are represented by a few unit catchments. For these reasons, a comparison of time series of averaged flood extent at the basin scale is more suited for an evaluation purpose.

The simulated time series compared well with observations at the basin scale during the 1993–2004 period with NS = 0.57, $r = 0.89$, and RE = 7%. In particular, the extreme events observed in 1997 and 1998, associated with El Niño and La Niña events, respectively (Fig. 11), are extremely well reproduced. However, note that the yearly maximum in simulated total flooded area is slightly overestimated when compared to observations, with larger discrepancies for 1999–2001. Moreover, model performance also varies regionally. For a more quantitative comparison, five other subregions are considered in order to evaluate the monthly averaged flooded areas over the 1993–2004 period: the central Amazonian floodplains (defined as the rectangle from 0°S–54°W to 8°S–72°W), and the Negro, Madeira, Xingu, and upper Solimões River basins. Among the five subregions defined within the Amazon basin, the best results were found for the Negro River basin, with relatively high correlation (0.85) and Nash–Sutcliffe coefficients (0.58), and low relative error (RE = −11%). In the central Amazon basin—which includes the Amazon River and parts of the Solimões, Negro, and lower Madeira River basins—the seasonality is well represented ($r = 0.85$), but the simulated flooded area is underestimated, on

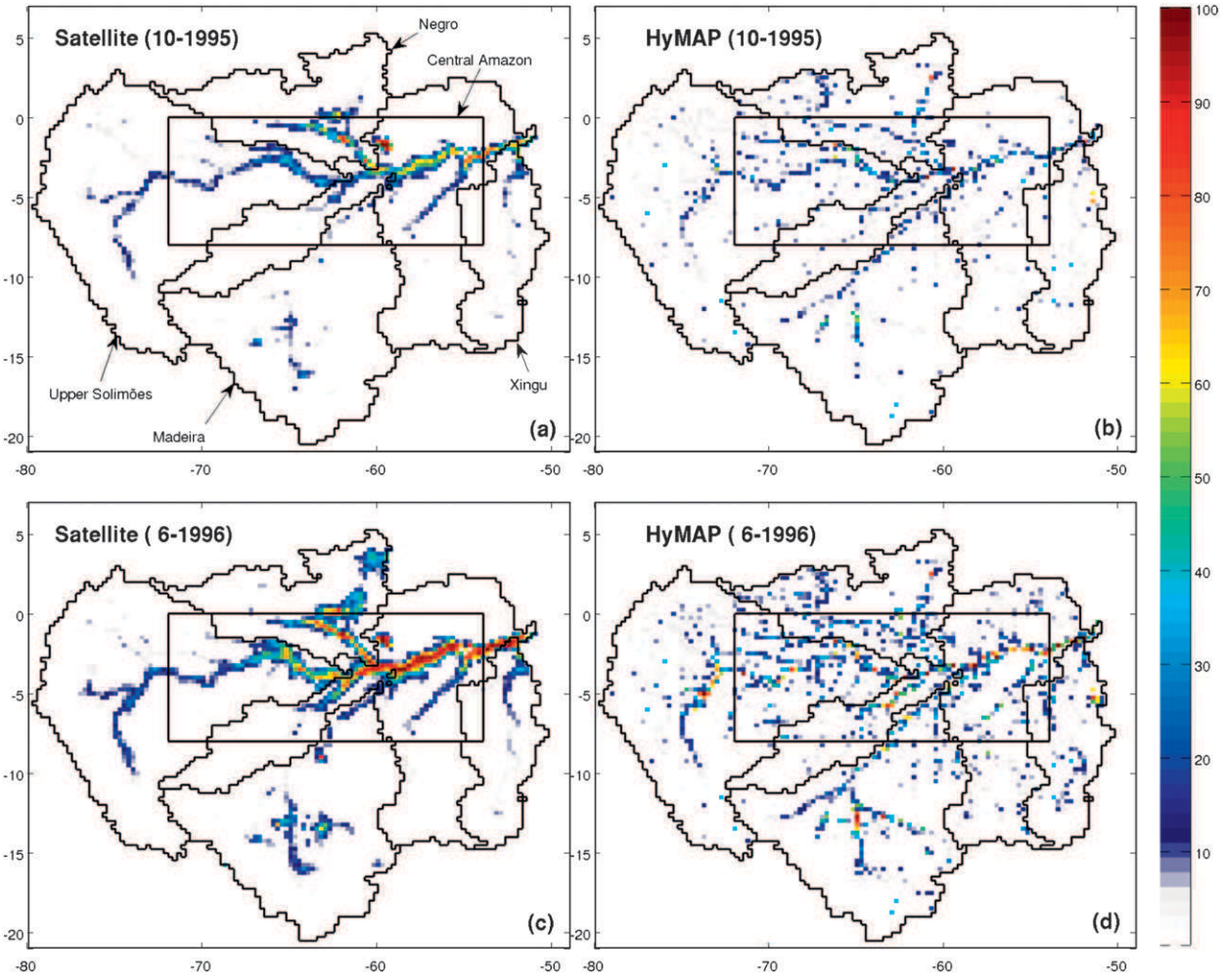

FIG. 10. Floodplain extent in the Amazon basin for (top) October 1995 and (bottom) June 1996. (left) Multisatellite observations (Papa et al. 2010) and (right) HyMAP outputs. Six regions considered to evaluate model outputs are contoured: the entire Amazon basin, central Amazonian floodplains (0°–8°S, 54°–72°W), and the Negro, Madeira, Xingu, and upper Solimões River basins. Units are in %.

average, by 21%. The underestimation found in the central Amazon and Negro River basins are compensated by an overestimation in other areas such as the upper Solimões and tributary river basins located in the lower Amazon basin, such as Xingu. In the upper Solimões River basin, seasonal variation is well represented (r = 0.84), although HyMAP overestimates flood extent in both wet and dry seasons (RE = 59%). Peaks are significantly overestimated in this region during the years 1993/94 and 1999–2001, leading to high peaks during the same periods at the basinwide scale. In the case of the Xingu River basin, modeled floodplain extent agrees with the satellite product during the dry seasons, but it is overestimated during the wet seasons, with a relative error (RE = 83%). Both Xingu and upper Solimões overestimate the amplitude and flooding during the wet seasons, explaining the low *NS* values.

To evaluate the interannual variability, anomalies of the floodplain extent averaged over the six regions are shown in Fig. 12. The correlation r and root-mean-square error (rmse) for each of the time series are also presented. Simulated monthly anomalies over the entire basin had r = 0.45 and rmse = 0.34, which demonstrate a reasonable improvement in comparison with Decharme et al. (2012) using ISBA–TRIP (r = 0.28 and rmse = 0.40). Regionally, r values vary from 0.37 (upper Solimões) to 0.69 (Madeira) and rmse from 0.33 (Xingu) to 0.84 (Madeira). The best overall simulation of monthly anomalies of floodplain extent is obtained again in the Negro River basin, with r = 0.58 and rmse = 0.50.

Differences between simulations and remote sensing–derived estimates may be due to different sources of uncertainty. First, uncertainties in the model parameterization might explain a large part of the differences.

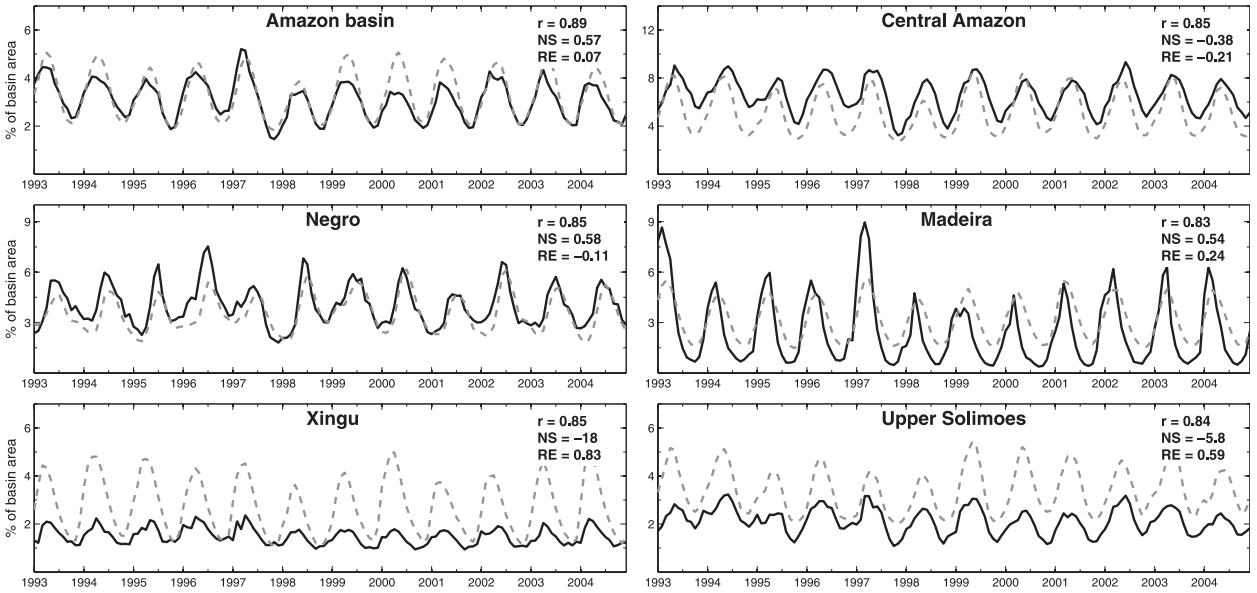

FIG. 11. Monthly averaged flooded extent over the 1993–2004 period for the six areas defined in Fig. 1. Model outputs are in dashed gray lines and satellite observations in black. The correlation (r), Nash–Sutcliffe coefficient (NS), and relative error (RE) are given for each series.

Previous evaluations of global-scale flow routing schemes have shown that the floodplain extent is very sensitive to changes in river geometry and roughness coefficient (Decharme et al. 2012; Yamazaki et al. 2011). Slightly reducing river depth and width can result in drastic increases in flooded areas, and vice versa. Inaccurate runoff and baseflow are other important sources of error in the flood extent simulation, over- or underestimating water stored in the river channels and, as a consequence, changing the floodplain dynamics. In addition, surface elevation errors, which are frequently found in current DEMs, can alter the relation (floodplain area × water level × water storage). The kinematic wave assumption can also impact the performance of simulated flood extent since it does not represent the backwater effects often present in certain locations of the Amazon basin.

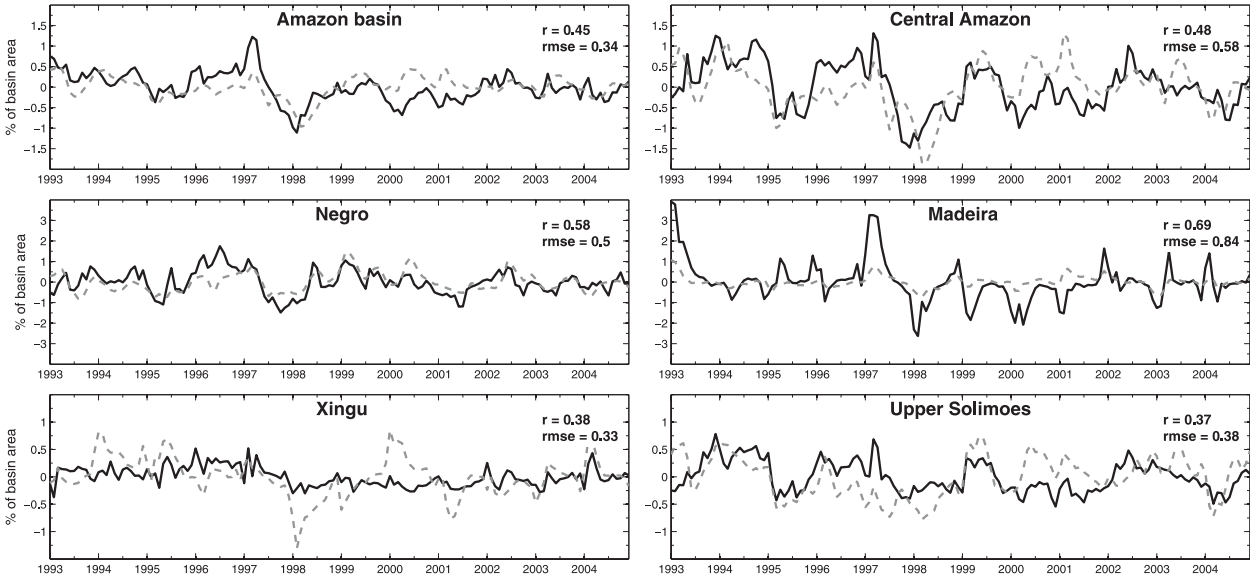

FIG. 12. As in Fig. 11, but for the monthly flooded area anomalies (mean seasonal cycle removed) and with the correlation (r) and the root-mean-square error (rmse) given for each series.

However, Yamazaki et al. (2011) show little difference in the basin-scale flood extent when kinematic and diffusive wave approaches are compared, suggesting that the kinematic wave assumption might have only a second order influence on floodplain dynamics. On the other hand, the satellite-derived products can also be sources of uncertainties. Prigent et al. (2007) and Papa et al. (2010) showed that the algorithm developed to retrieve floodplain extent from satellites still has difficulties in detecting inland water bodies covering less than ~80 km^2 of 25-km equal-area grid cells and it still has the tendency to underestimate small surface water-covered areas with less than 10% fractional coverage. The actual floodplain areas can be larger than those used as the reference.

e. Analysis of the water storage components

The understanding of the spatiotemporal distribution of water storage is essential to improved water resource management. HyMAP can provide useful insights of water storage in the different surface reservoirs within grid cells (runoff and baseflow time delays and river and floodplain reservoirs). According to the model outputs, as shown in Fig. 13, water is mainly stored in the runoff and baseflow ($R+B$) reservoirs at the basin scale, with a mean volume storage of 678 km^3. This means that 46% of the total runoff and baseflow derived from ISBA is flowing within grid cells before reaching the main river network. The water storage in $R+B$ reservoirs has a high amplitude, varying from about 260 up to 1220 km^3. The rivers store the second largest water volume in the Amazon basin, with about 41% (or 605 km^3) of the total runoff and baseflow. Finally, the average water storage in floodplains is about 13% (185 km^3). Water partitioning can be different in other regions within the Amazon basin according to physical characteristics of catchments and rivers.

Water stored in the central Amazon basin corresponds to 52% (765 km^3) of the total storage of the Amazon basin. This large volume is mainly stored in rivers, containing more than half (407 km^3) of the total water of this region. This is due to the large dimensions of the Amazon River and its tributaries within the selected area. In all other selected areas, $R+B$ reservoirs store the main water volume.

In the Negro River basin, water storage in rivers has a low amplitude compared to the water stored in the floodplain reservoir. This means that, once water reaches the river network, floodplain water storage is highly sensitive to the wet seasons. However, the $R+B$ reservoirs still represent the main water storage, with 57% (106 km^3) of the total runoff and baseflow produced in the basin. Floodplain water storage in the Madeira River basin is also sensitive to the wet seasons, with amplitudes higher than water storage in the rivers.

It must be highlighted that the water storage represented here corresponds to horizontal water fluxes only (i.e., runoff and baseflow). Other water reservoirs include soil moisture and precipitation intercepted by the vegetation canopy and are not discussed in this study. In addition, it should be noted that the values found here can vary significantly according to the parameter setting for river geometry.

f. Water discharge in floodplains

Figure 14 shows the annual cycles of simulated absolute water discharges in floodplains (Q_{fld}) and floodplain–river discharge fractions (Q_{frc}) averaged over the entire Amazon basin and the other five regions previously defined in Fig. 10. The Q_{fld} peaks vary from one region to another, according to the hydrological regime. The Madeira and Xingu River basins, located in the Southern Hemisphere, have Q_{fld} peaks in March–April. The Madeira River basin has the highest mean floodplain–river discharge fraction ($Q_{\text{frc}} = 7.8\%$), with peaks above 15% representing more than 400 m^3 s^{-1}, while the Negro River basin, located in the Northern Hemisphere, has the highest water discharge in floodplains in July–August (~450 m^3 s^{-1}) and has the second highest Q_{frc}, with a mean value of 7%, and peaks as high as 14%. The upper Solimões River basin is spatially distributed in both Hemispheres, resulting in peaks occurring in April–June. The presence of meaningful nonflooded areas in this region (according to model outputs, on average, only ~3% is covered with water) contribute to a low mean Q_{fld} of about 83 m^3 s^{-1}, corresponding to $Q_{\text{frc}} = 2.2\%$. Results are similar in the entire Amazon basin, with low mean Q_{fld} and Q_{frc} of ~128 m^3 s^{-1} and 3%, respectively. During wet seasons, Q_{fld} averaged over the entire Amazon basin is 280 m^3 s^{-1}, representing about 6% of the total water discharge, and in the dry seasons, Q_{fld} is reduced to values as low as 25 m^3 s^{-1}, or ~1% of the total water discharge. The highest Q_{fld} values occur in the central Amazon basin, where most floodplains are located. The mean Q_{fld} value in this region is 228.5 m^3 s^{-1} and peaks reach values above 500 m^3 s^{-1}. It must be highlighted that these values are averages for the entire regions and that Q_{fld} can be much higher in grid cells representing the main rivers. For example, the mean Q_{fld} values along the Solimões–Amazon main stream can be as high as 2750 m^3 s^{-1} (not shown). However, this discharge is negligible compared to the total water flow in the same reach (171 200 m^3 s^{-1}), resulting in a low Q_{frc} value of 1.6%. In contrast, a previous study based on the Muskingum method (Richey et al. 1989) estimated that up to 30% of the discharge of the Amazon River is routed through the floodplains. However, to the knowledge of the authors, no observed floodplain discharge is

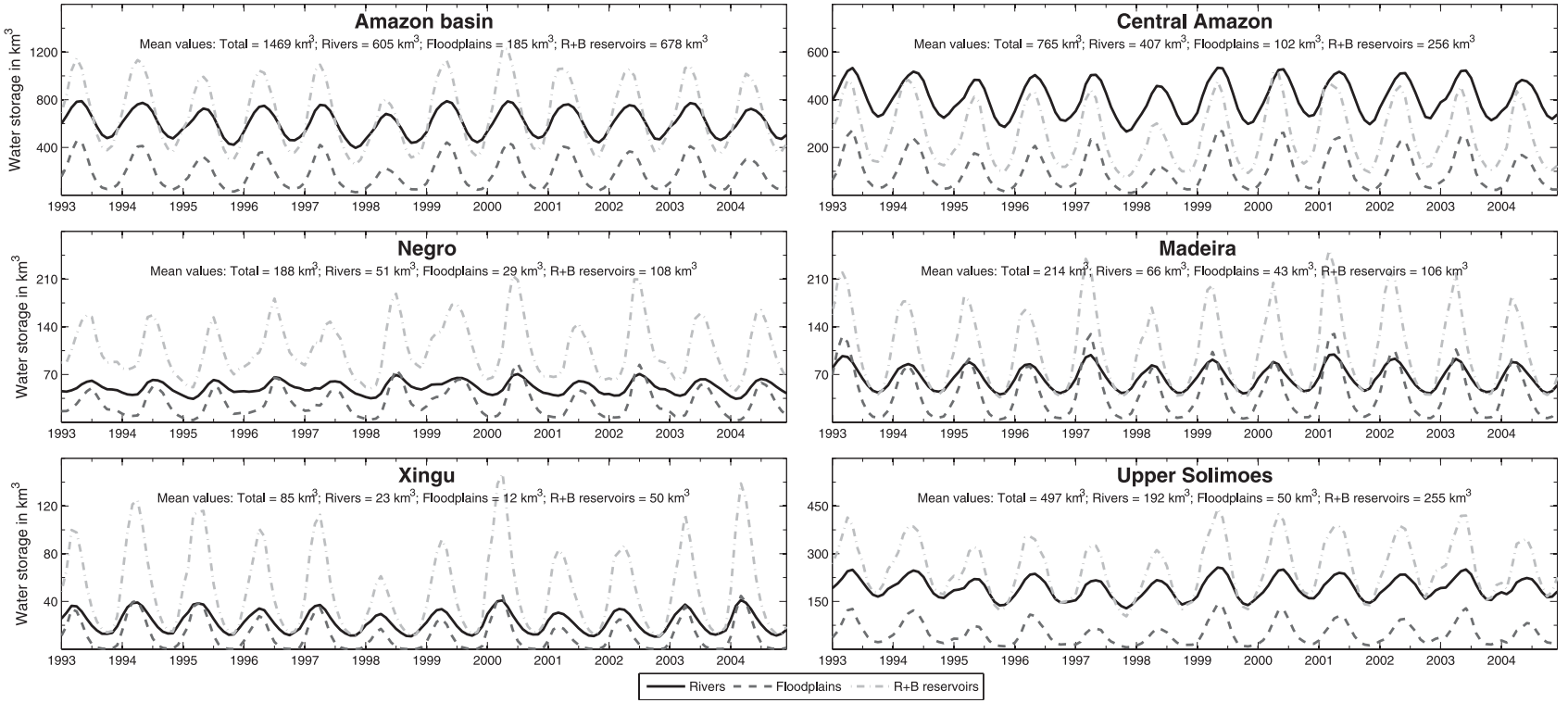

FIG. 13. Monthly water storage in the river, floodplain, and surface $R+B$ reservoirs in the Amazon basin and other five regions.

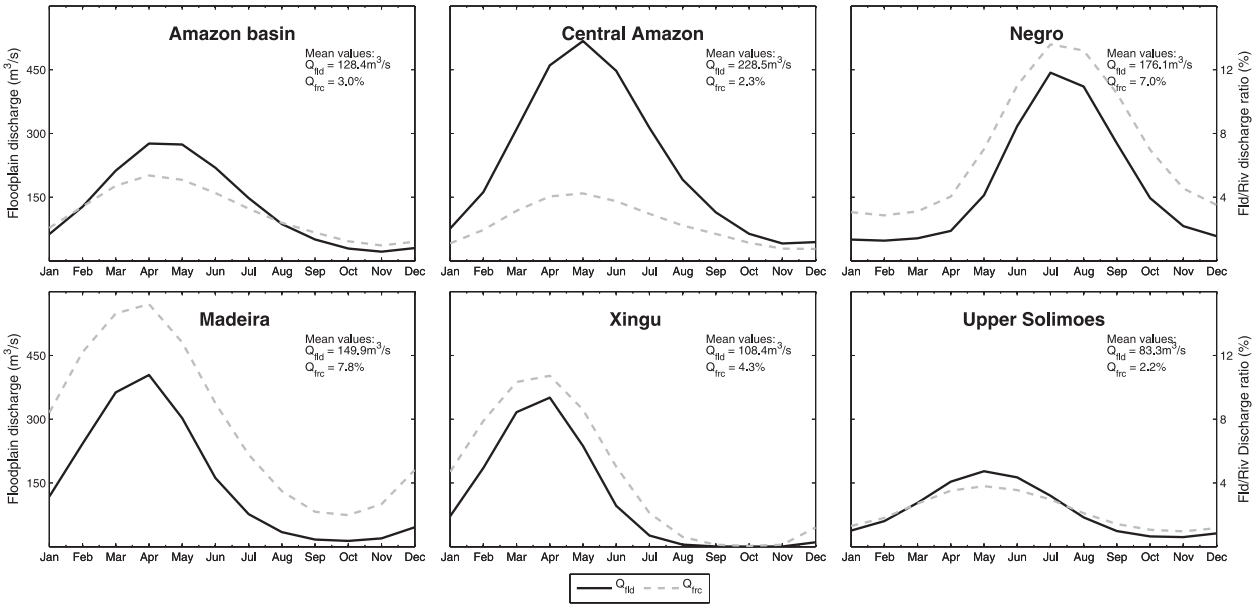

FIG. 14. Annual cycles of simulated floodplain water fluxes averaged for the Amazon basin and other five regions. Solid lines represent absolute water discharge discharges (Q_{fld}) in $\text{m}^3\ \text{s}^{-1}$ and dashed lines floodplain–river discharge fraction (Q_{frc}) in %.

currently available, and thus it is not feasible to confirm these estimates.

g. *Evaporation from open waters*

The total evapotranspiration from ISBA averaged over the entire Amazon basin is about 2.8 mm day^{-1} while the potential evaporation from open waters, derived from the modified Penman–Monteith equation without surface resistance [Eq. (17)], is 3.4 mm day^{-1}. Following Eq. (18), the remaining energy for evaporation from open waters E_w is 0.8 mm day^{-1}. This rate is valid for the case where the basin surface area is completely covered with water during the entire study period. However, as discussed before, open waters in the basin represent 2%–5% of the total surface area, resulting in low mean E_w values across the basin. As shown in Fig. 15, maximum and minimum E_w values simulated by HyMAP and averaged for the Amazon basin occur in April (~0.034 mm day^{-1}) and July–August (~0.013 mm day^{-1}), respectively.

Mean rates can be much higher in some locations, corresponding to an open water surface area. Monthly E_w values can be as high as 1.2 mm day^{-1} in some locations of the southern Madeira River basin in both dry and wet seasons. Other areas in the central Amazon basin can also have monthly rates above 1 mm day^{-1} during the wet seasons. Considering the differential evaporation from open waters has a relatively low effect on the water discharge at the scale of the entire Amazon basin (the mean E_w rate simulated by HyMAP is ~0.02 mm day^{-1}, representing ~1600 $\text{m}^3\ \text{s}^{-1}$ or about 0.8% of the total water discharge produced in the basin). However, even if evaporation from open waters may not be significant compared to the water discharge in the Amazon basin, it has been shown that E_w has a significant impact in the water balance in arid regions such as the Niger River basin (e.g., Decharme et al. 2012).

h. *Effects of floodplain dynamics on water discharge*

To evaluate the effects of floodplain dynamics on water discharge, two experiments have been proposed: (i) no dynamics in flooded areas (NODYN) [$v_f = 0$ in Eq. (11)] (i.e., floodplains are merely considered as river overflow reservoirs, following the same approaches as those in current versions of ISBA–TRIP and CaMa–Flood) and (ii) floodplains are completely removed from the system (NOFLD) (i.e., water flows only through rivers). The previously presented model output is considered as the reference simulation (SIM). An evaluation is performed at four gauging stations along the Solimões–Amazon River (Óbidos, Jaturana+Careiro, Manacapuru, and Tabatinga), as shown in Fig. 16.

At Óbidos, NS coefficients provided by NODYN (NS = 0.84) and NOFLD (NS = 0.78) are lower than those resulting from SIM. Flood waves are delayed by about 20 days at Óbidos when water flow in floodplains is not considered. This is caused by the increased water storage in floodplain reservoirs, which smooths and delays the hydrographs. Increases in water storage in floodplains slightly increases E_w rates and reduces volume errors (DV = 4.9%) in comparison with SIM

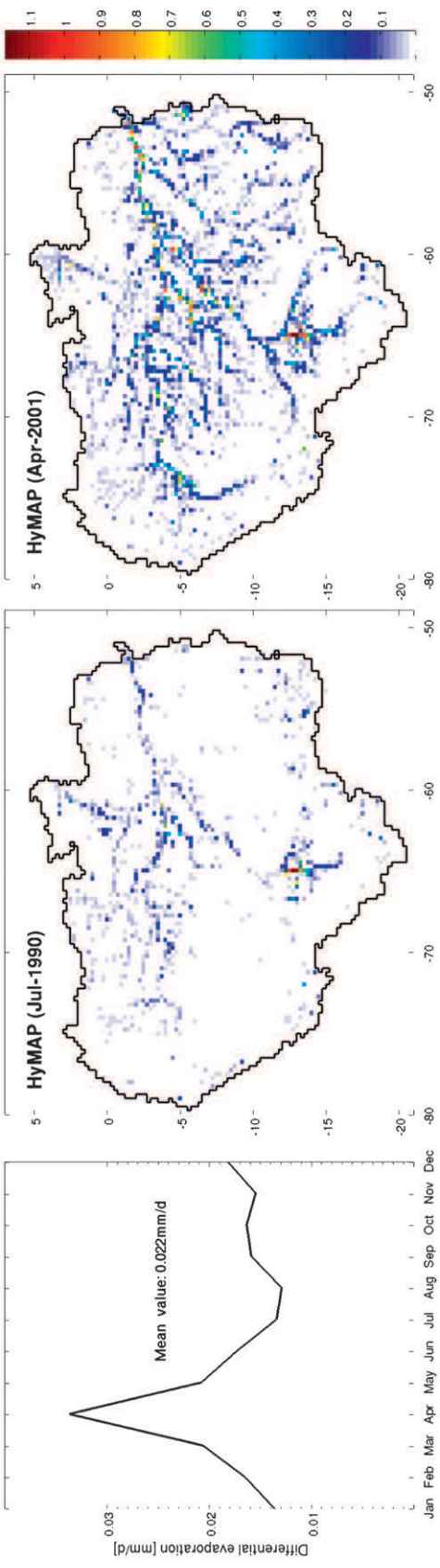

FIG. 15. Simulated evaporation from open waters (E_w). (left) The E_w annual cycle as simulated by HyMAP averaged to the entire Amazon basin. Mean E_w rates simulated by HyMAP for (middle) July 1990 (low evaporation rate) and (right) April 2001 (high evaporation rate). Units are in mm day^{-1}.

(DV = 5.1%). The opposite effect is seen for NOFLD. Neglecting floodplains results in an 18-day advance of the flood wave provoked by a significant augmentation of water storage in rivers and therefore of water depths h and flow velocity v (as discussed in section 4d, the flow velocity v is directly proportional to h). Since open waters are significantly reduced, an increasing of volume error (DV = 5.8%) is seen for NOFLD. Results at Jatuarana+Careiro are similar, with reduced NS values for both NODYN (0.81) and NOFLD (0.75), differences in time lags (DI values equal to 11 and −19 days, respectively), and volume errors (DV values equal to −6.3% and −5.7%, respectively). A slight increase of NS values is observed at Manacapuru with the experiment NODYN (NS = 0.82), probably caused by the change of time delay (DI = 9 days). NOFLD at Manacapuru has the same characteristics which were found at the other gauging stations with reduced NS (0.66), negative DI (−20 days), and higher DV (−5.2%). At Tabatinga station, the noise introduced by neglecting floodplain storage does not prevent obtaining a better NS (0.48) value with NOFLD. This is explained by the reduced time lag obtained in this experiment (DI = 16 days). Poor results are obtained with NODYN with NS close to zero and DI = 49 days.

5. Conclusions

This paper presents the Hydrological Modeling and Analysis Platform (HyMAP), a new parameterization of horizontal water flow over continental surfaces capable of routing surface runoff R and baseflow B provided by LSMs in offline mode. The model is a result of the integration and improvement of known approaches described by previous state-of-the-art global FRS and new features suggested in this paper, which include the representation of time delays for both R and B, the use of the kinematic wave equation to route water in rivers and floodplains separately, and the evaporation from open waters.

HyMAP was run for the Amazon basin at the daily time step and a 0.25° spatial resolution. A full evaluation of main variables such as water discharge and level, floodplain extent, and flow velocity is performed against a large dataset of in situ observations and satellite-derived products. In addition, water discharge in floodplains, evaporation from open waters, storage in reservoirs, and impact of floodplain dynamics on simulated water discharges are presented and discussed.

Results show that the model simulates well the discharge and water levels in the main rivers of the Amazon basin, with an overall performance better than previous modeling attempts. Nevertheless, as discussed in this

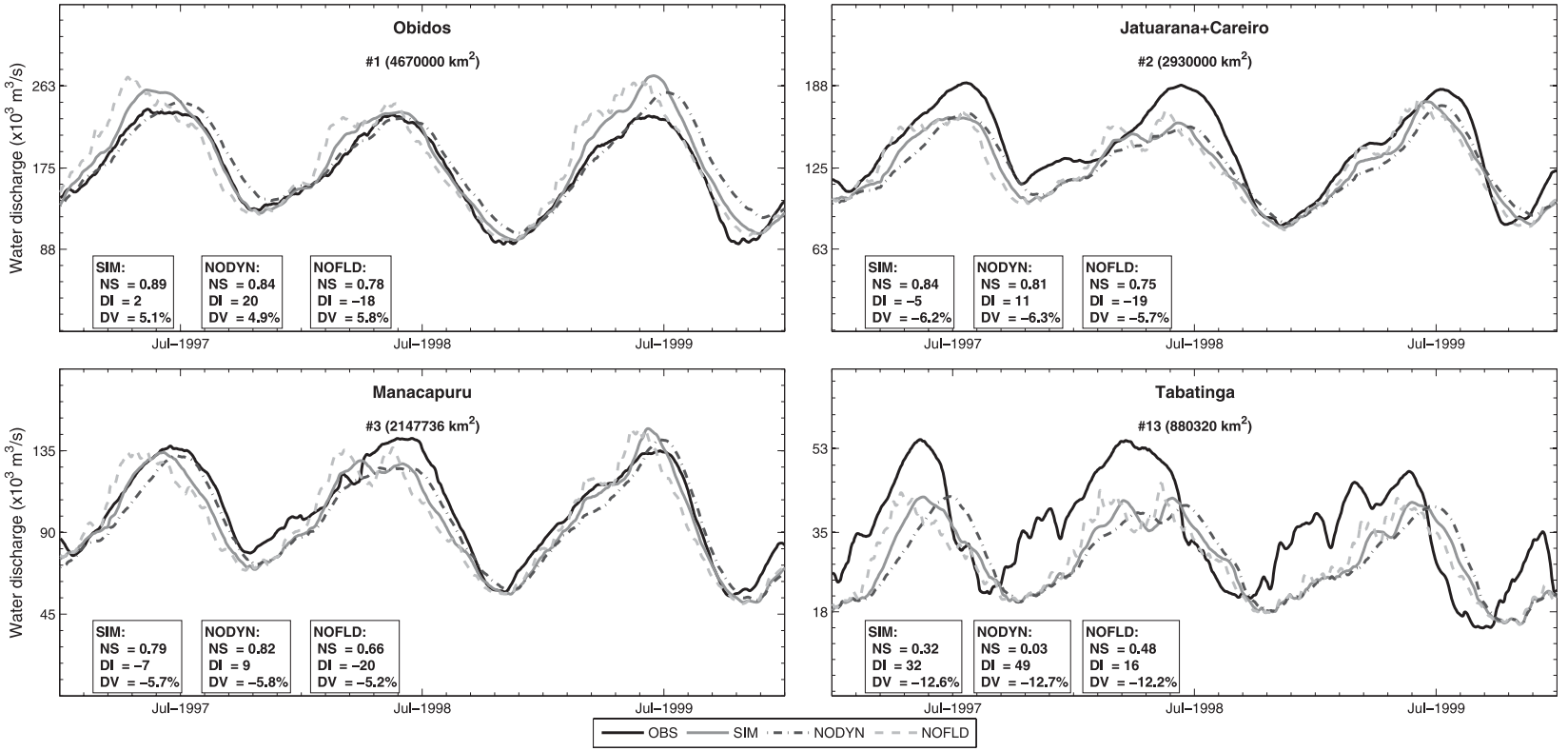

FIG. 16. Hydrographs at four gauging stations along the Solimões–Amazon River (Óbidos, Jaturana+Careiro, Manacapuru, and Tabatinga) resulting from experiments evaluating effects of floodplain dynamics on water discharges.

paper, smaller catchments present problems mainly related to scale issues and forcing errors. This happens because, as a general rule, the larger the studied domain, the coarser the spatial resolution and the more the processes must be simplified. Moreover, the lack of adequate global datasets prevents a better parameterization of the baseflow time delay (T_b) and river geometry (i.e., river width W and length L). These parameters account for most of the surface water stored in the basin, thus representing the major reservoirs.

For the first time, simulated flow velocity was evaluated against observations over the entire Amazon basin. Even though HyMAP and previous modeling attempts are similar, it has been shown that simulated v presents significant errors, possibly owing to uncertainties in the river geometry and simplifications of physical processes. Other sources of error are the kinematic wave assumption, which is not capable of simulating hysteresis caused by backwater effects in flat water surfaces. This limitation can also explain uncertainties in water levels and, to a lesser degree, in the floodplain extent. On the other hand, the use of a diffusive wave approach requires a much finer temporal resolution in order to avoid numerical instabilities. A choice for the kinematic wave equation was made in this study. However, further analyses must be performed to fully evaluate the limitations of each approach.

Satellite-derived and simulated interannual variability of floodplain extent matches well at the basin scale. However, significant differences can be noticed locally. Indeed, open water surfaces are closely dependent on river geometry and topography. The geometry defines whether river overflow may occur and the topography, which prescribes floodplain surface profile within a grid cell, determines the flooded area given an overflowed water volume. But both of them present limitations owing to problems with the needed input data.

Current satellite-based DEMs are not adequate to provide accurate floodplain elevation profiles. The SRTM30 DEM used to represent the topography and processed with FLOW to provide hydrological information has large uncertainties. For example, SRTM30 DEM data over South America have a mean absolute height accuracy of 1.7 m, with 90% of the errors being less than 7.5 m (Rodriguez et al. 2005, 2006). A few attempts have been proposed in the literature to reduce the SRTM30 uncertainty by degrading the spatial resolution (e.g., Wilson et al. 2007) and using land cover maps to identify the presence of forests (e.g., Coe et al. 2008). However, DEM errors remain as one of the main sources of uncertainty in modeling the interactions between rivers and floodplains.

Another issue that plays an important role in flooded areas is the model spatial resolution. Even relatively higher spatial resolutions may not adequately represent wide floodplains with only one grid cell, and as a consequence, open water extents are underestimated. For such cases, two-dimensional approaches capable of simulating floodplain water flow among neighboring grid cells might be necessary. These techniques have been largely used at smaller scales (e.g., Estrela and Quintas 1994; Horritt and Bates 2002) and must be adapted for use in global models in the future. Another solution is the use of DEM processing approaches called "burning methods" to change floodplain flow directions to correspond to the closest river stream. In particular, the floodplain burning approach, which takes into account river and floodplain maps, can be an efficient way to gradually change high-resolution DEM pixel elevations in flooded areas (Getirana et al. 2009a,b). This would concentrate the whole floodplain extent of a given river reach in only one grid cell.

It has been shown that about 3% of the water found the river network in the Amazon basin flow through the floodplains. This is the first estimate at the basin scale since other large-scale flow routing schemes do not take into account water dynamics in floodplains. Also, discharge estimates through floodplains are highly sensitive and limited by numerous aspects related to model parameters representing river geometry, flow dynamics, and DEM errors, and these results must be considered as first estimates.

However, as DEM precision and model physics improve, this value may change. In addition, the assimilation of two-dimensional water surface dynamics provided by SWOT will significantly refine floodplain water flow simulations. Briefly, when compared to previous global flow routing schemes, HyMAP shows visible improvements in simulating horizontal water flow over the continents and its use in general water resources studies and flood hazards is recommended.

This study has been developed as part of the SWOT (Alsdorf et al. 2007) Virtual Mission and the choices of the dynamics and processes included in HyMAP have been made, in some measure, to be able to use SWOT data. Current developments in the framework of this study include the use of an optimization scheme considering different data sources, such as radar altimetry, to improve the modeling, understanding, and streamflow forecasts in poorly gauged or ungauged basins (Getirana et al. 2012). Future applications include the development of a water height change assimilation approach using data provided by the SWOT mission (Mouffe et al. 2011). Also, the model is currently being implemented in the Land Information System (LIS) (Kumar et al. 2006). This effort is the first step to have HyMAP running in online mode with a variety of LSMs and climate models.

Acknowledgments. The first author would like to thank the Centre National d'Études Spatiales (CNES) for the financial support. The study benefited from data made available by Agência Nacional de Águas (ANA) and by the European Space Agency (ESA) under the form of Geophysical Data Records (GDRs). The multimission database of GDRs is maintained by the Centre de Topographie des Océans et de l'Hydrosphère (CTOH) at LEGOS. Grateful acknowledgments are also due to G. Cochonneau (IRD), M.C. Gennero (LEGOS), and R. Alkama (Météo-France) for their help in data acquisition and processing and P. Bates (Univ. Bristol) and an anonymous reviewer for their valuable comments.

REFERENCES

Alsdorf, D. E., E. Rodríguez, and D. P. Lettenmaier, 2007: Measuring surface water from space. *Rev. Geophys.,* **45,** RG2002, doi:10.1029/2006RG000197.

Arora, V. K., and G. J. Boer, 2001: Effects of simulated climate change on the hydrology of major river basins. *J. Geophys. Res.,* **106** (D4), 3335–3348.

——, F. H. S. Chiew, and R. B. Grayson, 1999: A river flow routing scheme for general circulation models. *J. Geophys. Res.,* **104** (D12), 14 347–14 357.

Bamber, J. L., 1994: Ice sheet altimeter processing scheme. *Int. J. Remote Sens.,* **15**, 925–938.

Biancamaria, S., P. D. Bates, A. Boone, and N. M. Mognard, 2009: Large-scale coupled hydrologic and hydraulic modelling of the Ob river in Siberia. *J. Hydrol.,* **379,** 136–150, doi:10.1016/j.jhydrol.2009.09.054.

Bousquet, P., and Coauthors, 2006: Contribution of anthropogenic and natural sources to atmospheric methane variability. *Nature,* **443,** 439–443, doi:10.1038/nature05132.

Chow, V. T., 1959: *Open-Channel Hydraulics.* McGraw-Hill, 680 pp.

Coe, M. T., M. H. Costa, and E. A. Howard, 2008: Simulating the surface waters of the Amazon River basin: Impacts of new river geomorphic and flow parameterization. *Hydrol. Processes,* **22,** 2542–2553, doi:10.1002/hyp.6850.

Cogley, J. G., 2003: GGHYDRO—Global hydrographic data, release 2.3. Trent Tech. Note 2003-1, 11 pp. [Available online at http://people.trentu.ca/~gcogley/glaciology/index.htm.]

Crétaux, J. F., and Coauthors, 2011: SOLS: A lake database to monitor in the near real time water level and storage variations from remote sensing data. *Adv. Space Res.,* **47,** 1497–1507.

Dadson, S. J., I. Ashpole, P. Harris, H. N. Davies, D. B. Clark, E. Blyth, and C. M. Taylor, 2010: Wetland inundation dynamics in a model of land surface climate: Evaluation in the Niger inland delta region. *J. Geophys. Res.,* **115,** D23114, doi:10.1029/2010JD014474.

Decharme, B., R. Alkama, F. Papa, S. Faroux, H. Douville, and C. Prigent, 2012: Global off-line evaluation of the ISBA-TRIP flood model. *Climate Dyn.,* **38** (7–8), 1389–1412, doi:10.1007/s00382-011-1054-9.

Döll, P., F. Kaspar, and B. Lehner, 2003: A global hydrological model for deriving water availability indicators: Model tuning and validation. *J. Hydrol.,* **270,** 105–134, doi:10.1016/S0022-1694(02)00283-4.

Dunne, T., L. A. K. Mertes, R. H. Meade, J. E. Richey, and B. R. Forsberg, 1998: Exchanges of sediment between the flood plain and channel of the Amazon River in Brazil. *GSA Bull.,* **110,** 450–467.

Estrela, T., and L. Quintas, 1994: Use of GIS in the modelling of flows on floodplains. *Proceedings of the Second International Conference on River Flood Hydraulics,* Wiley, 177–189.

Getirana, A. C. V., M.-P. Bonnet, and J.-M. Martinez, 2009a: Evaluating parameter effects in a DEM 'burning' process based on land cover data. *Hydrol. Processes,* **23,** 2316–2325, doi:10.1002/hyp.7303.

——, ——, O. C. Rotunno Filho, and W. J. Mansur, 2009b: Improving hydrological information acquisition from DEM processing in floodplains. *Hydrol. Processes,* **23,** 502–514, doi:10.1002/hyp.7167.

——, A. Boone, and N. Mognard, 2012: Automatic calibration of a flow routing scheme constrained by radar altimetry data. *Extended Abstracts, 20 Years of Progress in Radar Altimetry Symp.,* Venice, Italy, European Space Agency, 119. [Available online at http://www.congrexprojects.com/docs/12c01_docs/20ypra_abstracts_12_08_27_v9.pdf.]

Hagemann, S., and L. Dümenil, 1998: A parameterization of lateral water flow for the global scale. *Climate Dyn.,* **14,** 17–41.

Horritt, M. S., and P. D. Bates, 2002: Evaluation of 1D and 2D numerical models for predicting river flood inundation. *J. Hydrol.,* **268,** 87–99, doi:10.1016/S0022-1694(02)00121-X.

Kirpich, Z. P., 1940: Time of concentration of small agricultural watersheds. *Civ. Eng.,* **10,** 362.

Krinner, G., 2003: Impact of lakes and wetlands on boreal climate. *J. Geophys. Res.,* **108,** 4520, doi:10.1029/2002JD002597.

Kumar, S. V., and Coauthors, 2006: Land information system: An interoperable framework for high resolution land surface modeling. *Environ. Modell. Software,* **21,** 1402–1415, doi:10.1016/j.envsoft.2005.07.004.

Lehner, B., and P. Döll, 2004: Development and validation of a global database of lakes, reservoirs and wetlands. *J. Hydrol.,* **296,** 1–22.

Masson, V., J.-L. Champeaux, C. Chauvin, C. Meriguet, and R. Lacaze, 2003: A global database of land surface parameters at 1-km resolution in meteorological and climate models. *J. Climate,* **16,** 1261–1282.

Masutomi, Y., Y. Inui, K. Takahashi, and U. Matsuoka, 2009: Development of highly accurate global polygonal drainage basin data. *Hydrol. Processes,* **23,** 572–584.

Melack, J. M., L. L. Hess, M. Gastil, B. R. Forsberg, S. K. Hamilton, I. B. T. Lima, and E. M. L. M. Novo, 2004: Regionalization of methane emissions in the Amazon basin with microwave remote sensing. *Global Change Biol.,* **10,** 530–544.

Miller, J., G. Russell, and G. Caliri, 1994: Continental scale river flow in climate models. *J. Climate,* **7,** 914–928.

Mohamed, Y. A., B. J. J. M. van den Hurk, H. H. G. Savenije, and W. G. M. Bastiaanssen, 2005: Impact of the Sudd wetland on the Nile hydroclimatology. *Water Resour. Res.,* **41,** W08420, doi:10.1029/2004WR003792.

Mouffe, M., A. C. V. Getirana, S. Ricci, C. Lion, S. Biancamaria, N. Mognard, A. Boone, and P. Rogel, 2011: Towards SWOT data assimilation for hydrology: Automatic calibration of global flow routing model parameters in the Amazon basin. American Geophysical Union, Fall Meeting 2011, Abstract H23G-1364.

Noilhan, J., and J.-F. Mahfouf, 1996: The ISBA land surface parameterisation scheme. *Global Planet. Change,* **13** (1–4), 145–159, doi:10.1016/0921-8181(95)00043-7.

Oki, T., and Y. C. Sud, 1998: Design of total runoff integrating pathways (TRIP)—A global river channel network. *Earth Interact.,* **2**. [Available online at http://EarthInteractions.org.]

Paiva, R. C. D., W. Collischonn, and D. C. Buarque, 2012: Validation of a full hydrodynamic model for large-scale hydrologic modelling in the Amazon. *Hydrol. Processes,* doi:10.1002/hyp.8425, in press.

Papa, F., C. Prigent, F. Aires, C. Jimenez, W. B. Rossow, and E. Matthews, 2010: Interannual variability of surface water extent at the global scale, 1993–2004. *J. Geophys. Res.,* **115,** D12111, doi:10.1029/2009JD012674.

Portmann, F. T., S. Siebert, and P. Döll, 2010: MIRCA2000—Global monthly irrigated and rainfed crop areas around the year 2000: A new hight-resolution data set for agricultural and hydrological modeling. *Global Biogeochem. Cycles,* **24,** GB1011, doi:10.1029/2008GB003435.

Prigent, C., F. Papa, F. Aires, W. B. Rossow, and E. Matthews, 2007: Global inundation dynamics inferred from multiple satellite observations, 1993–2000. *J. Geophys. Res.,* **112,** D12107, doi:10.1029/2006JD007847.

Richey, J. E., L. A. K. Mertes, T. Dunne, R. Victoria, B. R. Forsberg, A. C. F. N. S. Tancredi, and E. Oliveira, 1989: Source and routing of the Amazon River flood wave. *Global Biogeochem. Cycles,* **3,** 191–204.

Rodriguez, E., C. S. Morris, J. E. Belz, E. C. Chapin, J. M. Martin, W. Daffer, and S. Hensley, 2005: An assessment of the SRTM topographic products. Jet Propulsion Laboratory Tech. Rep. JPL D-31639, 143 pp.

——, ——, and ——, 2006: A global assessment of the SRTM performance. *Photogramm. Eng. Remote Sens.,* **72,** 249–260.

Sausen, R., S. Schubert, and L. Dumenil, 1994: A model of river runoff for use in coupled atmosphere-ocean models. *J. Hydrol.,* **155,** 337–352.

Sheffield, J., G. Goteti, and E. F. Wood, 2006: Development of a 50-year high-resolution global dataset of meteorological forcings for land surface modeling. *J. Climate,* **19,** 3088–3111.

Shuttleworth, W. J., 1993: Evaporation. *Handbook of Hydrology,* D. Maidment, Ed., McGraw-Hill, 1–4.

Vörösmarty, C. J., B. Moore III, A. L. Grace, and M. P. Gildea, 1989: Continental scale models of water balance and fluvial transport: An application to South America. *Global Biogeochem. Cycles,* **3,** 241–265.

Wilson, M., P. Bates, D. Alsdorf, B. Forsberg, M. Horritt, J. Melack, F. Frappart, and J. Famiglietti, 2007: Modeling large-scale inundation of Amazonian seasonally flooded wetlands. *Geophys. Res. Lett.,* **34,** L15404, doi:10.1029/2007GL030156.

Yamazaki, D., T. Oki, and S. Kanae, 2009: Deriving a global river network map and its sub-grid topographic characteristics from a fine-resolution flow direction map. *Hydrol. Earth Syst. Sci.,* **13,** 2241–2251, doi:10.5194/hess-13-2241-2009.

——, S. Kanae, H. Kim, and T. Oki, 2011: A physically based description of floodplain inundation dynamics in a global river routing model. *Water Resour. Res.,* **47,** W04501, doi:10.1029/2010WR009726.

——, C. A. Baugh, P. D. Bates, S. Kanae, D. E. Alsdorf, and T. Oki, 2012: Adjustment of a spaceborne DEM for use in floodplain hydrodynamic modeling. *J. Hydrol.,* **436–437,** 81–91.